

# Delineation of subsurface variability in clay-rich landslides through spectral induced polarization imaging and electromagnetic methods

Jakob Gallistl<sup>a,\*</sup>, Maximilian Weigand<sup>b</sup>, Margherita Stumvoll<sup>c</sup>, David Ottowitz<sup>d</sup>, Thomas Glade<sup>c</sup>, Adrián Flores Orozco<sup>a</sup>

<sup>a</sup> Geophysics Research Division, Department of Geodesy and Geoinformation, TU-Wien, Gußhausstraße 27-29, E120-3, 1040 Vienna, Austria

<sup>b</sup> Department of Geophysics, University of Bonn, Meckenheimer Allee 176, 53115 Bonn, Germany

<sup>c</sup> ENGAGE – Geomorphological Systems and Risk Research, Department of Geography and Regional Research, University of Vienna, Universitätsstraße 7, 1010 Vienna, Austria

<sup>d</sup> Geological Survey of Austria, Department of Geophysics, Vienna, Austria

## ARTICLE INFO

### Keywords:

Electromagnetic induction (EMI) mapping  
Induced polarization (IP) imaging  
Clay-rich landslide  
Spectral induced polarization  
Flysch Zone

## ABSTRACT

Although commonly triggered by heavy or long-lasting precipitation events, landslides in clay-rich formations are hardly predictable as their triggering mechanisms are still not fully understood. Hence, detailed information about the internal structure of landslides with high spatial resolution is fundamental for an improved understanding of triggering mechanisms and management. In this context, electrical resistivity tomography (ERT) is a well-established method used for the delineation of lithological interfaces in landslides and changes in water content. However, the quantitative interpretation of the ERT images can be challenging, particularly for clay-rich landslides, considering that the electrical signatures are dominated by the variations in the clay fraction rather than saturation. Moreover, large scale investigations also demand the development of faster surveying techniques. Hence, in this study we discuss the combined investigation of a landslide with low induction number electromagnetic (EMI) mapping and induced polarization (IP) imaging. We investigate the application of such methods to assess subsurface variability across different scales: near surface EMI mapping and their correlation with geomorphological data, whereas IP images are used to investigate the extension at depth from the shallow structures. Measurements are performed at a shallow clay-rich landslide in Lower Austria (Austria), characterized by lithological structures of the Flysch and Gresten Klippen Zone, with both formations known to be highly susceptible to landsliding. The interpretation of the imaging results for data collected along 15 profiles is performed using separately acquired hydrogeological and geotechnical data. We observe a relationship between the electrical properties and geotechnical parameters which permits to delineate areas associated to different weathering stages controlling the groundwater flow. Moreover, spectral induced polarization (SIP) data collected along one transect shows sensitivity to changes in textural composition, such as the fraction of clay minerals. The study shows the suitability of an integrated investigation with EMI mapping and IP imaging in combination with extensive geotechnical data for an improved characterization of subsurface variability and thus, understanding of clay-rich landslides.

## 1. Introduction

Landslides in urban settlements are global socio-economic geohazards, particularly those developed in clay-rich formations due to their hardly predictable acceleration and liquefaction phases as well as high sediment volumes (Malet et al., 2005). Landslide mobilization typically occurs as a result of intense and long-lasting precipitation which can lead to a build-up of positive pore-pressure and an associated reduction of shear strength, particularly for clayey and silty textures (Campbell,

1975; Rogers and Selby, 1980). Hence, knowledge of the internal structure and textural composition of landslides is an important prerequisite for hydrogeologic and hydraulic modelling (e.g. the deduction of water-circulation within the landslide body), which is further needed for the understanding of internal processes associated with triggering mechanisms (Merritt et al., 2014). Traditionally, direct ground-based hydrogeological and geotechnical measurements, using piezometers, inclinometers, dynamic probing and laboratory textural analysis from soil samples have been used to provide information on the subsurface

\* Corresponding author.

E-mail address: [jakob.gallistl@geo.tuwien.ac.at](mailto:jakob.gallistl@geo.tuwien.ac.at) (J. Gallistl).

properties of landslides (Glade et al., 2001, 2005; Petley et al., 2005; Perrone et al., 2014). However, such investigation techniques are spatially constrained to specific point locations and require spatial up-scaling, which, particularly for heterogeneous areas, is associated with an undesirable increase in data uncertainty (Binley et al., 2015; Wainwright et al., 2016). This lack of spatial resolution may be mitigated by the use of geophysical techniques (e.g., Jongmans and Garambois, 2007), which permit to gain quasi-continuous information about subsurface physical properties, which in turn are linked to hydrogeological (e.g., Binley et al., 2005; Weller et al., 2015), lithological (e.g., Hack, 2000; Bell et al., 2006) and geotechnical parameters (e.g., Cosenza et al., 2006; Sass et al., 2008; Fressard et al., 2016). Of such geophysical methods, electromagnetic induction (EMI) and induced polarization (IP) imaging appear as promising techniques for the investigation of clay-rich landslides, considering their ability to solve for the subsurface distribution of the electrical properties, which are strongly linked to clay and water content and can be used to derive hydrogeological information (e.g., Grandjean et al., 2011; Sirles et al., 2012; Merritt et al., 2014; Altdorff and Dietrich, 2014).

The EMI method has relatively low application costs and, more importantly, is a contactless technique well-suited to map large areas in relatively short acquisition times (e.g. Everett, 2012; Doolittle and Brevik, 2014; Binley et al., 2015). EMI measurements provide depth-integrated values of the in-phase and quadrature components of the secondary EM field, which in turn can be transformed into apparent electrical conductivity  $\sigma_a$  (Eca) given a low-induction number assumption. The resulting bulk Eca can then be interpreted in terms of clay content, porosity, temperature changes, electrolyte salinity and water saturation given a calibrated petrophysical relationship (Brevik et al., 2006). EMI methods are widely used in soil studies (Doolittle and Brevik, 2014), and monitoring measurements can be applied for the quantification of soil moisture changes (Robinson et al., 2012; Shanahan et al., 2015). It has been suggested that in the scope of slope instability studies, maps of  $\sigma_a$  permit the identification of zones with different soil properties relevant for the characterization of infiltration and surface run-off regimes (e.g., Kušnirák et al., 2016). Hence, a few studies have referred to the application of EMI techniques for the characterization of landslides (e.g., Mauritsch et al., 2000; Grandjean et al., 2011; Altdorff and Dietrich, 2014; Kušnirák et al., 2016). Moreover, the application of airborne electromagnetics (AEM) has drawn attention as a suited technique to investigate areas at the large scale (Nakazato and Konishi, 2005; Lysdahl et al., 2017).

However, typical geophysical investigations of landslides target the delineation of both the vertical and lateral distribution of physical properties, as needed, e.g., for the delineation of the sliding plane or the estimation of mobilized volumes. On that account, electrical resistivity tomography (ERT) is a method which permits to solve for the subsurface distribution of electrical resistivity (or its inverse electrical conductivity) in 2D and 3D models and it has been extensively applied in the last 20 years for the characterization of landslides (see Perrone et al., 2014 for an overview). Resistivity images can be explored for resistivity contrasts, which can be indicative for lithological changes and thus, the sliding materials and the stable unit and the geometry of the sliding plane (Lapenna et al., 2003; Bell et al., 2006), as well as the areas in the landslide characterized by higher water content (e.g., Lebourg et al., 2005; Sass et al., 2008; Lehmann et al., 2013). However, clay-rich sediments are also related to low electrical resistivity values due to conduction mechanisms taking place at the negatively-charged surface of clay minerals (e.g., Revil and Glover, 1998). Hence, the quantitative interpretation of the ERT results may be challenging, taking into account the impossibility to discriminate whether the electrical conductivity models are controlled by variability in water or clay content. Hence, some authors have referred to the application of the Induced Polarization (IP) method for the structural characterization of landslides (Marescot et al., 2008; Perrone et al., 2014). The IP method is an extension of the ERT technique, which provides

information about the electrical conduction and capacitive (polarization) properties of the subsurface (e.g., Kemna et al., 2012 and references therein). Initially, the IP method was developed for mining applications due to the strong polarization response observed in the presence of iron sulphides (e.g., Pelton et al., 1978). However, in recent years it has emerged as a promising technique for hydrogeological and environmental applications (e.g., Kemna et al., 2012). Studies demonstrate the successful application of the IP method for an improved lithological discrimination (Kemna et al., 2004), the assessment of permafrost degradation (Doetsch et al., 2015), the monitoring of bioremediation processes (Flores Orozco et al., 2011, 2013), the mapping and characterization of contaminant plumes (Flores Orozco et al., 2012a; Ntarlagiannis et al., 2016), and the monitoring of microscale particle injections (Flores Orozco et al., 2015). Furthermore, IP laboratory measurements performed at different frequencies, in the so-called spectral IP (SIP), have shown a characteristic frequency dependence of the IP effect linked to textural parameters of soil (e.g., Binley et al., 2005; Weller et al., 2010; Revil et al., 2012). Based on such findings, there is an extensive research into the application of the SIP method to characterize the hydraulic conductivity (Slater, 2007; Weller et al., 2015). Nevertheless, the mechanisms underlying the IP response are still not fully understood (e.g., Kemna et al., 2012); thus correlation with ground-truth information is required for an adequate interpretation of the IP imaging results.

To date, only a limited number of studies report the application of the IP method for the characterization of landslides (Marescot et al., 2008; Taboga, 2011; Sastry et al., 2012; Dahlin et al., 2013; Sirles et al., 2013). However, in such studies the evaluation of the IP images is mostly based on cross-validation with other geophysical data or limited lithological information provided by core drillings. Geotechnical testing such as penetration tests or textural analysis of recovered sediments have not been considered for a quantitative interpretation of the IP imaging results. Furthermore, and to the best of our knowledge, no studies have yet reported the application of SIP imaging for the characterization of landslides. Hence, we believe that a case study presenting extensive (S)IP imaging results and their evaluation through geomorphological and geotechnical data is required to better assess the applicability of this technique for an improved investigation of landslides.

To fill this gap, we present here a case study for the characterization of a landslide in Lower Austria through a combined investigation of EMI and IP mapping and geotechnical data. The landslide is characterized by high fractions of clay-rich sediments of the Flysch and Klippen Zone (Wessely et al., 2006), which imposes some limitations on the investigations based solely on ERT results. Through extensive geotechnical information available at the study area, we evaluate the geophysical results and their applicability to determine relevant landslide characteristics such as the accumulation and infiltration zones, the sliding plane, and ground water flow paths. Available information about textural soil parameters allow us to discuss the value of the additional information gained from the capacitive properties of the subsurface provided by the IP method. Furthermore, we present SIP imaging results to investigate the frequency dependence of the subsurface electrical properties and their correlation with geotechnical and textural parameters. In the next section, we provide a description of the study area as well as the geophysical and non-geophysical data, followed by the presentation and discussion of EMI maps. Then we present and discuss the IP imaging results and the SIP data, as well as their correlation with ground-truth data, followed by the final interpretation of the geophysical investigation and the conclusions.

## 2. Site description

The study area is located in the southwestern part of Lower Austria, Austria (Fig. 1). Several investigations have been carried out at the study area by the local authorities, thereby gathering extensive

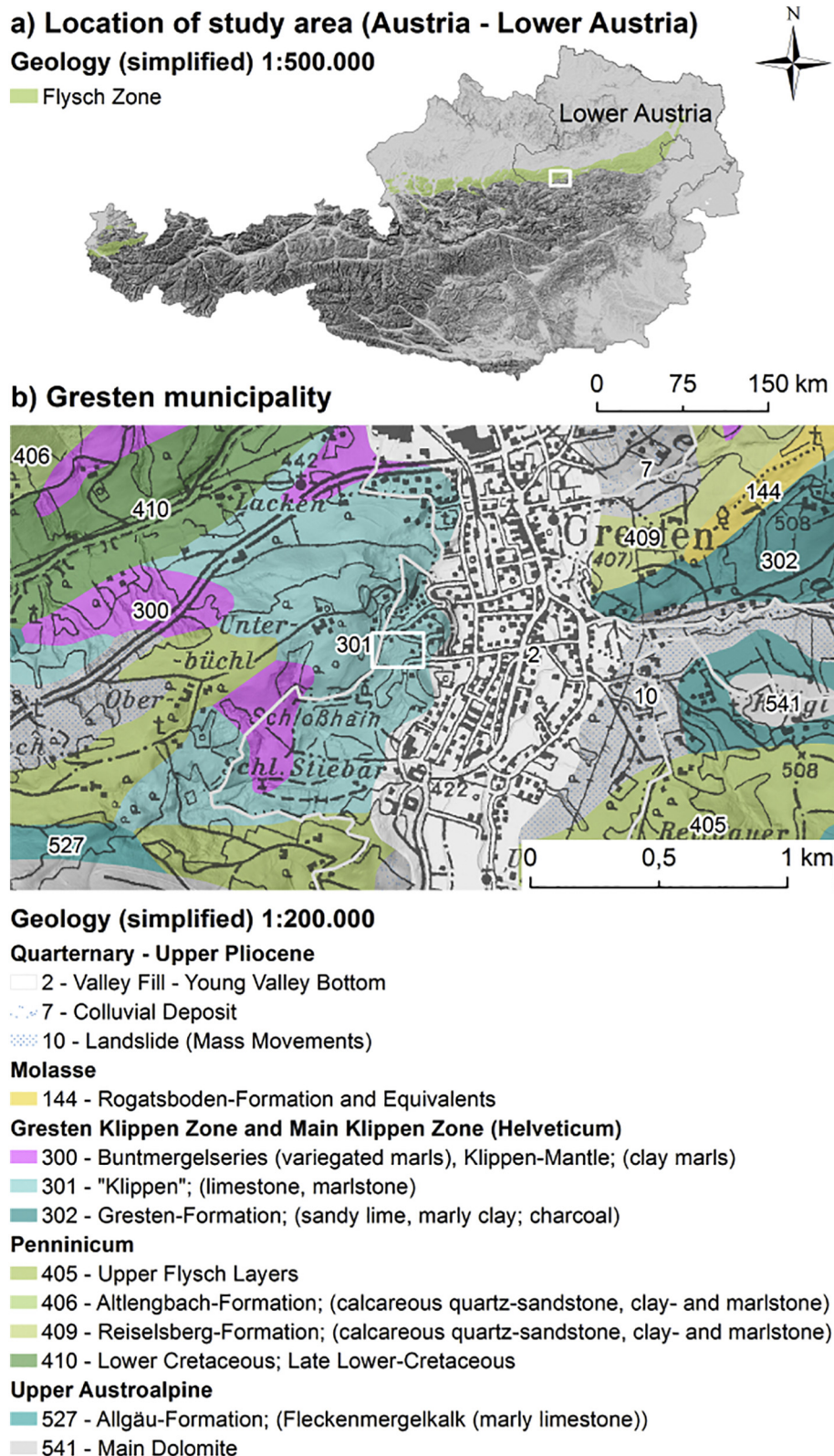


Fig. 1. Location of the study area in the geological unit of the (Rhenodanubian) Flysch Zone in the western part of Lower Austria, Austria (1a). Geological setting of the study area (1b). Geological maps modified after Weber (1997) and Schnabel et al. (2002).

information about the surface deformation by means of geomorphological mapping, geodetic monitoring techniques and terrestrial laser scanning. Further subsurface investigations have been conducted through direct methods, namely dynamic probing heavy, percussion drilling and inclinometer measurements. Variations in the groundwater

level and soil moisture have been measured using a piezometric network and time-domain reflectometry (TDR) respectively. Previous geotechnical investigations at the study area have suggested the existence of a shallow sliding plane in approximately 2–3 m depth (for further details refer to Canli et al. (under revision)).

Based on geomorphological mapping the extension of the active landslide area has been estimated to cover approx. 4000 m<sup>2</sup>. The inclination of the slope ranges between 5° and 15°, with steeper parts up to 20° in the bulged areas, which are related to the recently most active sections. The geological setting of the study area is characterized by three different tectonic units: (i) the Penninic (Rhenodanubian) Flysch Zone (FZ) in the north, (ii) the (Upper) Austroalpine Northern Calcareous Alps (NCA) in the south, (iii) and the Helvetic unit of the Gresten Klippen Zone (GKZ) in between. Such compound settings result in diverse lithological contacts, which promote landslide occurrence in the region (e.g., Ruttner and Schnabel, 1988; Schnabel et al., 2002). From 1100 landslides reported in Lower Austria between 1965 and 2006, 62% of them occurred in the Flysch and Klippen Zones (42% Flysch Zone and 20% Klippen Zone) (e.g., Gottschling, 2006; Petschko et al., 2014). The GKZ and FZ units are intricate regarding their stratigraphy, lithology and facies, with both units mainly characterized by marine sandstones, clays, clayey shales, marly shales and marly limestones, yet conglomerates and breccia have been reported in the GKZ (for more details see, e.g., Ruttner and Schnabel, 1988; Wessely et al., 2006).

The first slope movement in the area was reported in 1975, and it has been suggested its triggering was related to heavy precipitation events occurring between June 29th and July 3th. The landslide was reactivated in 1978 after heavy precipitation on Mai 31th, with further displacements reported in 2006. Between 2007 and 2012, displacements were monitored via tachymetric surveys, which have been stopped after 2012 due to only minimal displacements observed (e.g., max. 20 cm in 2009). Since the first displacements occurred in 1975, remediation techniques at the site have included the removal of displaced material, filling of tension cracks and depletion zones (1975 and 1978), leveling of the upper area and the installation of a drainage system in the eastern part of the study area in 2009.

### 3. Material and methods

#### 3.1. Low induction number electromagnetic imaging

Electromagnetic induction (EMI) imaging results presented in this study were performed with the so-called terrain conductivity meters, or more precisely, low induction number electromagnetic methods (e.g., McNeill, 1980b; Everett, 2005). EMI exploits the principle of electromagnetic induction by making use of a sensor system that generates a primary magnetic field by applying an alternating current at a fixed frequency which passes through a transmitter coil. Due to the time-varying character of the magnetic field, eddy currents are induced in a conductive subsurface, which subsequently generate a secondary magnetic field sensed by the receiver coil. The induction number ( $b$ ) for a given system is a function of the angular frequency of the primary field ( $\omega$ ), the separation between the transmitter and receiver coils ( $l$ ), the magnetic permeability ( $\mu$ ) and the bulk electrical conductivity ( $\sigma$ ) of the earth, and can be written (e.g., McNeill, 1980a) as:

$$b = \mu\sigma\omega l^2 \quad (1)$$

Terrain conductivity meters are instruments where  $l$  and  $\omega$  are designed to work at low induction number ( $b < 1$ ), at which the response is dominated by the ratio between secondary and primary magnetic field. Assuming that  $\mu$  in subsurface materials is close to one as in vacuum, the measured response is then only controlled by the electrical properties, thus permitting to obtain the apparent electrical conductivity  $\sigma_a$  in the subsurface quasi in real time (Keller and Frischknecht, 1966; Ward and Hohmann, 1988). As a contactless technique EMI permits to map large areas in reasonably low acquisition times (up to 5000 m<sup>2</sup>/h depending on the study site).

Values of  $\sigma_a$  represent a nonlinear average of the electrical conductivity values of the examined (sensitive) volume across a depth range that depends on the coil separation and orientation (McNeill,

1980b). The transmitter and receiver coils can be orientated horizontally (horizontal coplanar, HCP) or vertically (vertical coplanar, VCP) with respect to the ground surface. Increasing  $l$  in combination with VCP loops increases the depth range for the  $\sigma_a$  measurement (e.g., McNeill, 1980b; Callegary et al., 2007). Modern commercial instruments typically provide more than one transmitter/receiver pair and therefore can provide  $\sigma_a$  for different depth ranges. Vertical profiles of the electrical conductivity ( $\sigma$ ) of the examined volumes can be obtained from inverse modelling (e.g., Mester et al., 2011; von Hebel et al., 2014) of  $\sigma_a$  data sets measured for different depths of investigation (i.e., varying coil separation, coil orientation).

#### 3.2. EMI mapping

In this study we applied EMI measurements to map lateral changes in subsurface electrical properties using the CMD-Explorer (by GF Instruments), which uses three receiver coils with separations of 1.48 m, 2.82 m, and 4.49 m to the transmitter coil simultaneously, at an operating frequency of 10 kHz. All measurements on the landslide were performed in VCP mode for effective depth ranges of 2.2 m, 4.2 m and 6.7 m. The sampling frequency was 1 Hz, hence at an average walking speed  $\sigma_a$  values were collected approximately every 0.7 m along the walking tracks presented in Fig. 2a. The measured conductivity values were geo-referenced by means of differential GPS measurements. In total, the data set consists of approximately 30,000  $\sigma_a$  values with the survey performed within 3 h. EMI measurements were planned to map the entire extension of the recently active landslide area and delineate lateral variations in the electrical conductivity. In this study, we do not discuss the inversion of EMI data and associated uncertainties, which is required to solve for vertical variations in  $\sigma_a$ . Instead, we present maps of the  $\sigma_a$  directly recovered from measurements recorded with different coil separations. The maps were obtained by spatially interpolating all positive measured  $\sigma_a$  values (negative values were removed) using the kriging method. For the interpolation we used a linear variogram and an elliptical search space stretching into the direction of the landslide movement (axis ratio 1:2).

#### 3.3. Complex conductivity imaging

Similar to ERT, the induced polarization (IP) method is based on four-electrode configurations, where two of them are used for current injection and the other two are used to record the resulting voltage. In case of frequency-domain, current injection is performed using a sinusoidal waveform and data collection includes the measurement of the ratio between the measured voltage and current, as well as the time delay between both, resulting in a complex-valued electrical transfer impedance. Measurements can be repeated at different frequencies to gain information about the frequency dependence of the electrical properties, in the so-called spectral IP (SIP). SIP measurements are commonly conducted at the low frequencies (between 10 mHz and 1 kHz), with low frequencies (< 1 Hz) associated to long acquisition times; whereas high frequencies (> 10 Hz) bear the risk of contamination of the data due to electromagnetic effects (Flores Orozco et al., 2013). In case of time-domain surveys, IP measurements record the remnant voltage after the current injection is switched off (e.g., Binley and Kemna, 2005). Both frequency and time-domain measurements are theoretically equivalent, coupled by a Laplace transformation, and can both be used to investigate the distribution of complex electrical conductivity in subsurface materials. (Flores Orozco et al., 2012a). A detailed review of the IP method can be found in Ward (1990; Binley and Kemna (2005), Kemna et al. (2012).

The low frequency electrical properties of the subsurface are commonly expressed in terms of the complex electrical conductivity  $\sigma^*(\omega)$  (with  $\omega$  denoting the angular excitation frequency), which can be parameterized by means of its real,  $\sigma'(\omega)$ , and imaginary,  $\sigma''(\omega)$  components, or by its magnitude  $|\sigma^*(\omega)|$  and phase-shift  $\varphi(\omega)$ , such that:

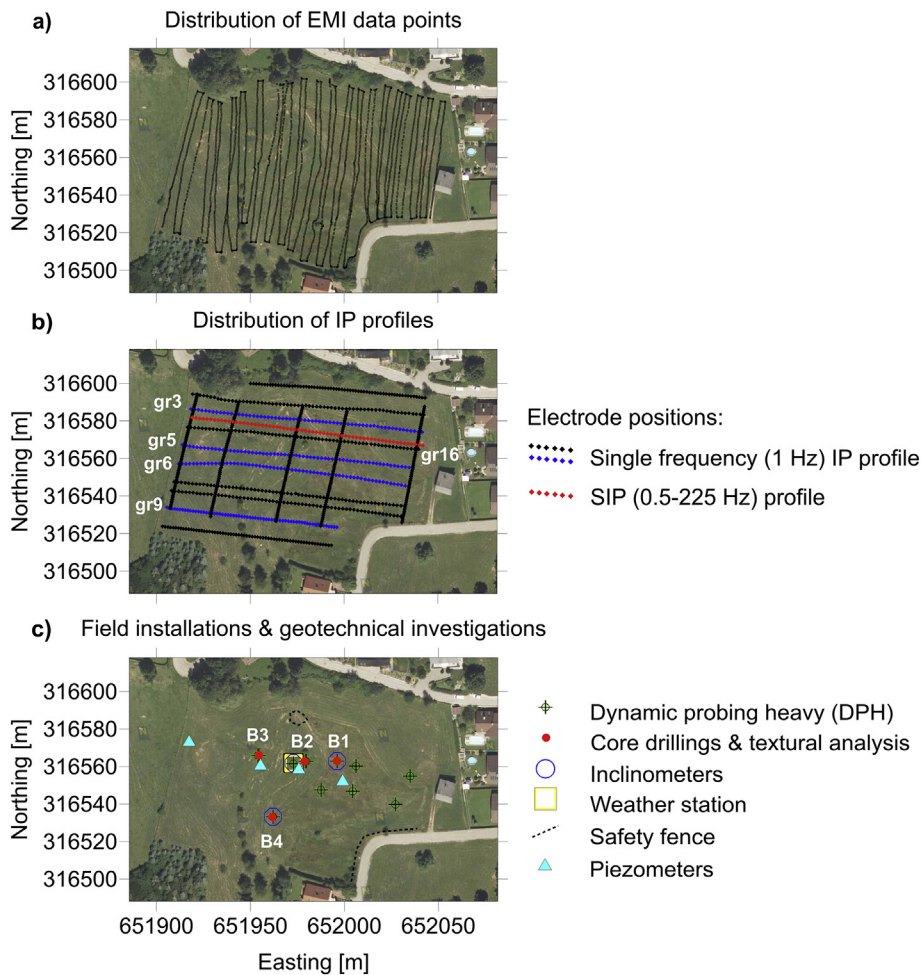


Fig. 2. Experimental set-up at the study area showing the transects for the collection of the EMI mapping data (indicated by the black dots in Fig. 2a), the orientation of the IP profiles (position of the electrodes indicated by the black, blue, and red symbols in Fig. 2b), and the location of the measuring points of direct methods, as well as field installations (2c). (For interpretation of the references to color in this figure legend, the reader is referred to the web version of this article.)

$$\sigma^*(\omega) = |\sigma^*(\omega)| e^{i\varphi} = \sigma'(\omega) + i\sigma''(\omega) \tag{2}$$

where  $i = \sqrt{-1}$ , and

$$\varphi = \arctan\left(\frac{\sigma''(\omega)}{\sigma'(\omega)}\right) \tag{3}$$

The real part of the complex conductivity accounts for energy loss (ohmic conduction) and, for sediments without metallic minerals, is mainly controlled by the porosity, connectivity of the pore space, saturation, and the fluid electrical conductivity of the pore-filling electrolyte (e.g., Revil and Glover, 1998; Lesmes and Morgan, 2001). The imaginary component is related to energy storage (polarization), which, in absence of metallic minerals, is given by: (1) the occurrence of clay minerals that can act as ion selective membranes, in the so-called membrane polarization (e.g., Titov et al., 2010; Bucker and Hördt, 2013; Hördt et al., 2017), and (2) electro-chemical polarization taking place at the electrical double layer (EDL), which is formed at the grain-fluid contact (e.g., Leroy et al., 2008; Leroy and Revil, 2009). In case of the membrane polarization the magnitude of the polarization effect is mainly a function of pore-space geometry (i.e., the sequence of wide and narrow pores and their pore lengths and radii), and for further details we refer to the studies of Bucker and Hördt (2013), Hördt et al. (2016), Chuprinko and Titov (2017), Hördt et al. (2017).

### 3.4. Inversion of IP imaging data sets

Inversion techniques are used to reconstruct the spatial distribution of complex conductivity from measured data. In this study, inversion of the IP data was performed using CRTomo, a complex resistivity inversion algorithm by Kemna (2000), using the sensitivity-controlled focusing (SCF) regularization scheme presented in Blaschek et al. (2008). This regularization scheme is based on the minimum gradient support (MGS) described by Portniaguine and Zhdanov (1999) and permits to solve for images with sharp contrast between structures characterized by different electrical properties, yet allowing smooth parameter changes within them (Blaschek et al., 2008). This is particularly important, as landslides are typically complex systems which cannot be explained by simple two layer cases without variations in the electrical properties within the layers. We opted for this regularization scheme, over the commonly used smooth-regularization, to properly solve for the interface between the sliding material and the bedrock, which is expected to form a sharp contrast between materials with contrasting electrical properties (e.g., Lapenna et al., 2003). Although CRTomo permits the definition of error models to fit the data to a confidence interval within the inversion (Kemna, 2000; Flores Orozco et al., 2012b), in case of data sets presented here we used robust inversion schemes based on an iterative re-weighting of poorly fitted data points (referred to as IRLS, e.g., Labrecque and Ward, 1990; Kemna, 2000), which are less sensitive to incorrect estimates of the random data error, as discussed in Morelli and Labrecque (1996). Model appraisal was

performed based on the analysis of cumulated sensitivity (e.g., the sum of absolute, data-error weighted sensitivities of all considered measurements), as performed in previous studies (Kemna et al., 2002; Weigand et al., 2017). Accordingly, we masked pixels in the imaging results associated to poor sensitivity, i.e., those pixels associated to  $\log_{10}$  cumulated sensitivities 2 orders of magnitude smaller than the highest cumulated sensitivity.

### 3.5. Single frequency IP mapping and SIP imaging

In this study, single frequency (1 Hz) IP imaging measurements were collected along 15 profiles distributed over the active landslide area: ten profiles orientated parallel to the landslide axis (west-east, WE), and five profiles perpendicular to it (north-south, NS), as depicted in Fig. 2b. Profiles collected in WE direction had an average distance of 10 m between them, using 64 electrodes in each profile with 2 m separation between electrodes. The profiles at the boundaries of the landslide (gr1, gr9, gr10) were collected with 1.5 m spacing between electrodes to avoid placing electrodes close to anthropogenic structures, commonly related to the contamination of IP data by cultural noise (e.g., Flores Orozco et al., 2012a). The separation between the NS profiles ranges between 20 and 40 m (Fig. 2b), with measurements collected with 64 electrodes and a separation of 1 m between electrodes in each profile. Aiming for a depth of investigation of 15 m, IP measurements were conducted with a dipole-dipole configuration combining skip-0, skip-1 and skip-2 protocols. The skip refers to the dipole length, defined by the number of electrodes skipped between the two current electrodes, as well as between the two potential electrodes (Slater et al., 2000). Such configuration permitted an acquisition time of 45 min (at 1 Hz), aiming for the collection of the 15 mapping IP profiles within 2.5 days from May 10th to 12th to warrant similar meteorological and subsurface conditions. Particular care was taken to avoid potential readings with electrodes previously used for current injection and the contamination of the data due to polarization of the electrodes (e.g., LaBrecque and Daily, 2008; Flores Orozco et al., 2012b).

To investigate the spectral behavior of the subsurface materials in the landslide, SIP data were collected along one profile in WE direction (gr16 in Fig. 2b) with 64 electrodes and 2 m separation between electrodes. Here, 12 frequencies in the range between 0.5 and 225 Hz were used with the same dipole-dipole configuration previously applied in the single-frequency surveys. All measurements were collected using a DAS-1 instrument (from MultiPhase Technologies), with the instrument placed at the center of the profile (between electrode 32 and 33). A control of the contact resistances between adjacent electrodes was performed before data collection, with the re-installation of electrodes performed in case of high values ( $> 1$  k $\Omega$ ), to ensure a good contact between electrodes and the ground, aiming for current injections in the range between 100 and 400 mA.

To illustrate the quality of the measured data, in Fig. 3a we present the pseudosection of the IP measurements in terms of the apparent resistivity ( $\rho_a$ ) and apparent phase-shift ( $\varphi_a$ ), for data collected along profile gr5, as well as their corresponding histograms. This particular profile was selected as it is expected to be representative for the study area and it is close to most of the geotechnical measurements, permitting a direct comparison with ground-truth information (c.f., Fig. 2b, c). Due to the nature of IP imaging measurements, pseudosections are expected to reveal smooth variations of  $\rho_a$  and  $\varphi_a$ , and abrupt changes may be indicative of a data set containing systematic errors, i.e., outliers, which need to be removed before the inversion. Plots in Fig. 4a reveal smooth variations in the pseudosection of  $\rho_a$ , with values ranging between 10 and  $\sim 80$   $\Omega\text{m}$ , without any observable outlier. In case of the  $\varphi_a$  readings, the pseudosection reveals mainly values between 0 and  $-10$  mrad for short dipole lengths (located at the shallow levels of the pseudosection). Measurements located at larger pseudodepth reveal poor spatial consistency with larger variations between adjacent

readings, suggesting readings with a poor signal-to-noise ratio (S/N). In order to remove outliers, we adapted the filtering approach proposed by Flores Orozco et al. (2018). The automatized data processing consists of a four step procedure: 1) the data set is partitioned into subsets defined by potential readings collected by the same current dipole, 2) the median  $\varphi_a$  for each subset is computed, as well as 3) the deviations to such median value ( $\Delta\varphi$ ) from each reading in the subset, 4) removal of all readings associated with an absolute deviation  $|\Delta\varphi|$  exceeding two times the standard deviation of  $\Delta\varphi$  of the entire data set. Furthermore, we analyse the distribution of the measurements. To this end, the remaining measurements are binned using the rule proposed by Sturges (1926) and Larson (1975), and further outliers are defined as those measurements located in bins separated from the main distribution. As discussed in Flores Orozco et al. (2018), the presence of gaps in the histogram indicates measurements without spatial correlation within the data set. Fig. 3b presents the pseudosections for  $\rho_a$  and  $\varphi_a$ , as well as the corresponding histograms, after following the steps defined above. Such plots show pseudosections less affected by outliers, with  $\varphi_a$  values ranging between  $-10$  and  $0$  mrad, with consistent results observed for the rest of the IP profiles (data not shown).

### 3.6. Complementary geotechnical and hydrogeological methods

At the landslide, dynamic probing heavy (DPH) was performed with a pneumatic heavy dynamic penetrometer (SRS-15), using a drop weight of 50 kg, a cone diameter of 43.7 cm and a drop height of 0.5 m, with the results presenting the blow counts needed to insert the probe for a 10 cm increment. In this study we present data collected along thirteen DPH soundings performed along the landslide axis, as depicted in Fig. 2c. Additional six core drillings (only four presented in this study) were retrieved from perforations with a maximum depth of  $\sim 9$  m in the vicinity of the DPH locations, as presented in Fig. 2c. Soil samples taken from the core drillings were analysed in the laboratory to gain the particle size distribution using sieving (based on ÖNORM L 1061-1/ DIN-ISO 3310/1) and sedimentation analysis (with reference to ÖNORM L 1061-2).

For the monitoring of subsurface displacement and the delineation of possible shear zones, one automatic chain inclinometer with an installation depth of 13 m, and two manual inclinometers with installation depths of 6.5 m, are operated at the study site, as presented in Fig. 2c. Measurements were taken for the sequential segments of 1 m for the 13 m inclinometer, whereas segments of 0.5 m were used for the 6.5 m inclinometers. Furthermore, variations in the groundwater levels are monitored by means of a piezometric network, with sensors installed to a depth of 7 and 8 m respectively (Fig. 2c). For more details on the geotechnical investigations at the study site we refer to Canli et al. (under revision).

## 4. Results and discussion

### 4.1. EMI mapping

Fig. 4 presents the interpolated maps of the apparent conductivity values for the three collected depth ranges (i.e., 2.2, 4.2, 6.7 m), in the following referred to as  $\sigma_{2.2}$ ,  $\sigma_{4.2}$ , and  $\sigma_{6.7}$ . We note here, that anomalously high  $\sigma_a$  values ( $> 40$  mS/m) are associated with the response of metal from anthropogenic structures and other measuring instruments (e.g., fences, inclinometers, and the weather station; c.f. Fig. 2c) and will not be further addressed.

In general maps for  $\sigma_{2.2}$  and  $\sigma_{4.2}$  reveal consistent patterns and  $\sigma_a$  values, permitting the identification of two main regions: (i) an area of elevated  $\sigma_a$  ( $> 25$  mS/m) in the central region of the landslide, as well as (ii) areas characterized by low  $\sigma_a$  values ( $< 20$  mS/m), located at the western and north-eastern regions of the site, corresponding to the highest ( $> 455$  m above sea level, asl) and lowest topography levels ( $< 440$  m asl) respectively, as observed in Fig. 4f. To evaluate the

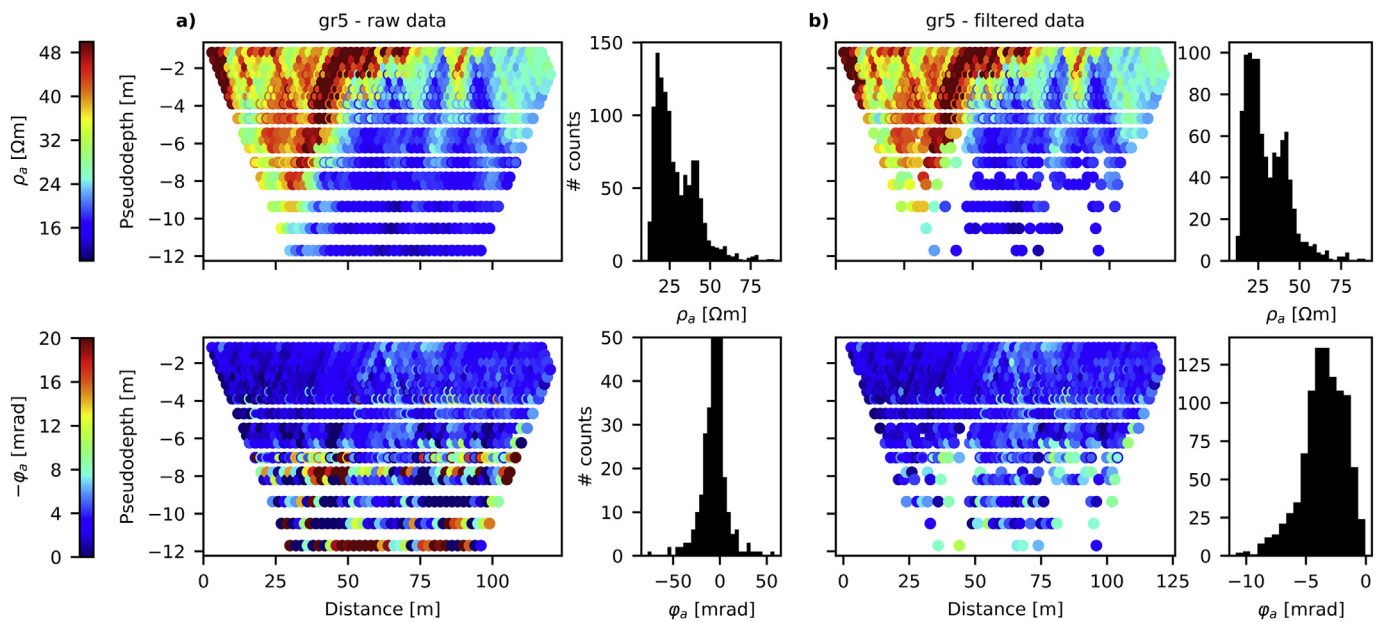


Fig. 3. Raw data analysis: Plots present the measured values in terms of the apparent resistivity (first row), and the apparent phase-shift (second row) for data collected along profile gr5 (Fig. 2b). Plots show the pseudosections and histograms for the raw data (Fig. 3a) and after the removal of outliers (Fig. 3b).

similitudes for the different depth ranges, in Fig. 4d and 4e we present difference images for consecutive depth ranges. Considering the minor differences between the maps of  $\sigma_{2,2}$  and  $\sigma_{4,2}$  (Fig. 4d), characterized by an only modest variation in  $\sigma_a$  ( $\sim 2$  mS/m), we can interpret only minimal vertical variations in shallow subsurface materials (between 0.5 and 4 m depth). Nevertheless, the map for  $\sigma_{6,7}$  reveals visible variations, in comparison with shallower maps, with a broader range in the measured  $\sigma_a$  values, as also evidenced in Fig. 4e.

Comparison of the shallow maps ( $\sigma_{2,2}$ ,  $\sigma_{4,2}$ ) and the  $\sigma_{6,7}$  map reveal two major differences: (i) a significant increase in the  $\sigma_a$  values for the central area of the landslide, suggesting an increase in saturation or clay content at depth in that area; as well as (ii) an increase in the variability of  $\sigma_a$  in the western part of the landslide, where higher  $\sigma_a$  values can be observed. Given the higher variability in  $\sigma_a$  observed in the deeper EMI measurements (Fig. 4c), we classify the  $\sigma_{6,7}$  maps into four main regions arranged in west-east direction: (1) a low conductivity region ( $< 20$  mS/m) related to topographical highest areas ( $> 455$  m asl), (2) a region of intermediate conductivity values ( $\sim 26$  mS/m), (3) a region of elevated conductivity values (30–38 mS/m) associated to topography values between 444 and 455 m asl, and (4) low to intermediate conductivity values (18–26 mS/m) located at the foot of the landslide ( $\sim 440$  m asl). A color-coded map using such classification is presented in Fig. 4g, which reveals consistent features to surface topographical discontinuities, as observed in the hillshade model of the DEM (Fig. 4f).

#### 4.2. Interpretation of the EMI mapping in combination with geomorphological data

The correlation between the changes in topography and the  $\sigma_a$  features suggests a link between the EMI maps and geomorphological patterns. To better investigate this, we overlapped the EMI maps with geomorphological features, namely, the limits of the landslide scarps, waterlogged areas and the accumulation zone as obtained from geomorphological mapping (Fig. 4a, b, c). Plots in Fig. 4 show in general that the three  $\sigma_a$  depth ranges solve consistently for high  $\sigma_a$  values in waterlogged areas, with an observed increase in  $\sigma_a$  with increasing the depth range (e.g., an increase from 30 to 40 mS/m for the waterlogged area in the center of the study site for the  $\sigma_{6,7}$  map). For waterlogged areas, which can be expected to be fully saturated, such increase in the electrical conductivity suggests an increase in clay content and thus, the

possible contact between units with different hydrogeological properties, a common factor associated to the accumulation of pore-water pressure and the triggering of landslides (e.g., Samyn et al., 2012). In particular, the observed change between the shallow-to-intermediate and the deep maps might be related to the contact to the shallow sliding plane delineated in a previous study located in approximately 2–3 m depth (Canli et al., under revision).

Yet, to interpret EMI maps at different depths, it is necessary to take into account the sensitivity at depth associated with the geometry of the instrument. The normalized sensitivity function  $\Phi$  for EMI measurements in the VCP mode can be computed using the well-known equation (McNeill, 1980b):

$$\Phi = \frac{4 \frac{D}{T}}{\left[4 \left(\frac{D}{T}\right)^2 + 1\right]^{\frac{3}{2}}} \tag{5}$$

in which  $D$  represents the depth as continuous variable. Plots for the instrument used in our study (Fig. 4h) reveal the highest sensitivity for  $\sigma_{2,2}$  and  $\sigma_{4,2}$  maps between  $\sim 0.25$  and 3 m depth, clearly demonstrating the influence of sliding materials, and shallow waterlogged areas, on the  $\sigma_a$  values. Whereas, deepest EMI measurements ( $\sigma_{6,7}$ ) are sensitive to depths between 0.5 and 4 m (Fig. 4h). Hence, the increase in  $\sigma_a$  values at depth for the central area of the landslide (c.f. Fig. 4e) seems to be related to the contribution of both the sliding materials and the stable unit.

The different landslide scarps show a spatial correlation with lateral variations in the  $\sigma_a$  values in all EMI maps. Furthermore,  $\sigma_a$  patterns observed also in all EMI maps are consistent with the location of the accumulation zone, which in the case of  $\sigma_{6,7}$  is characterized by a transition from high ( $\sim 36$  mS/m) to intermediate ( $\sim 28$  mS/m) conductivity values. The slightly lower conductivity values of the materials in the accumulation zone could be explained by the higher degree of compaction as a result of the accumulating pressure from sliding downhill.

#### 4.3. Interpretation of IP imaging in combination with soil-physical and geotechnical data

##### 4.3.1. Single frequency IP

For completeness, the evaluation of the resolved complex

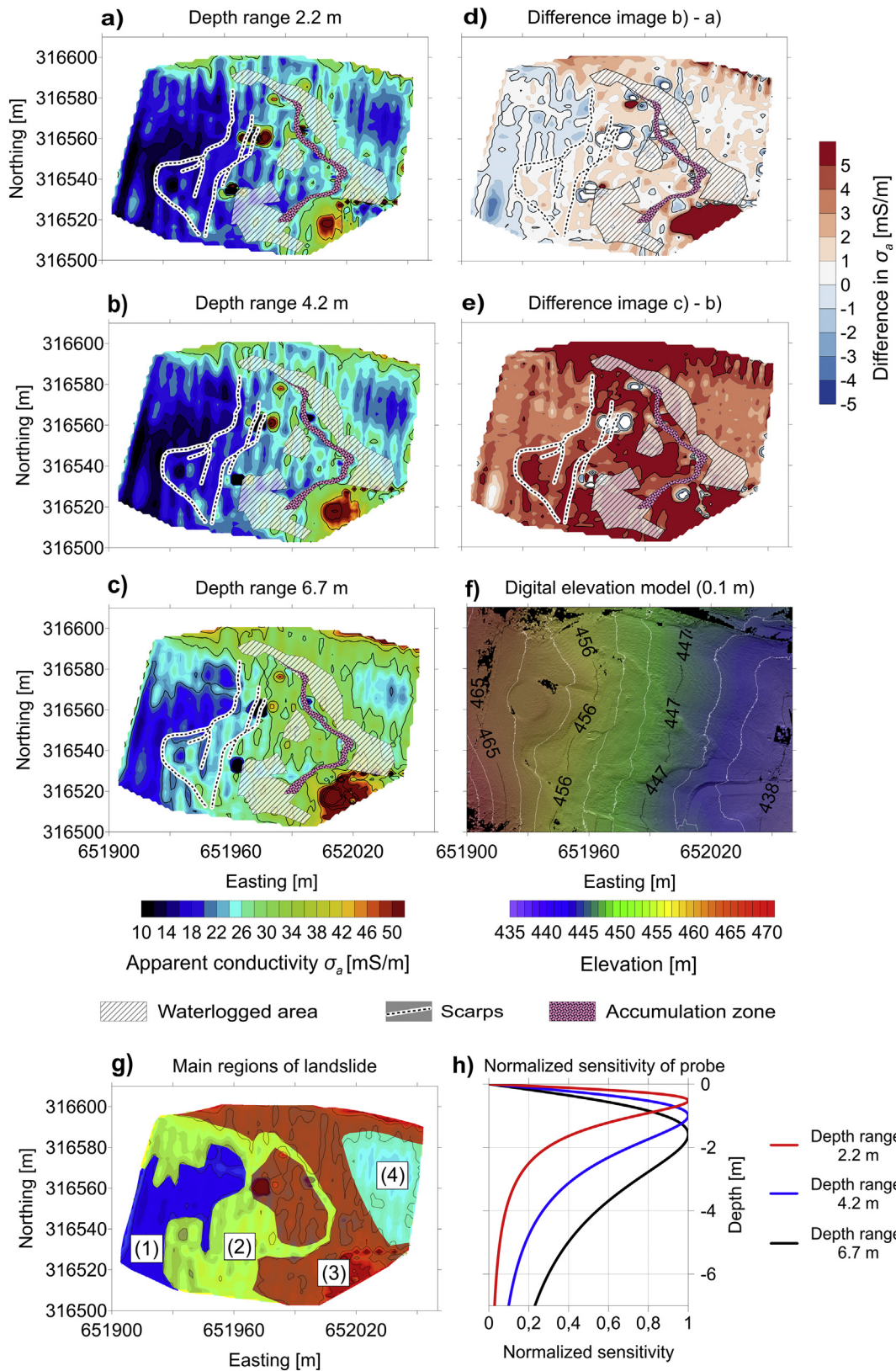


**Fig. 4.** EMI maps of the apparent electrical conductivity corresponding to the depth ranges of 2.2, 4.2, 6.7 m (Fig. 4a, b, c respectively), with the geomorphological features superimposed over the  $\sigma_a$  maps. Difference images for the  $\sigma_a$  maps for the depth ranges 2.2 and 4.2 m (4d) and 4.2 and 6.7 m (4e) are also presented to evaluate changes at different depth. The DEM (4f) of the landslide and the main regions interpreted from  $\sigma_a$  maps (4g) are presented for comparison. Plots of the normalized sensitivity function for the three depth ranges (4h).

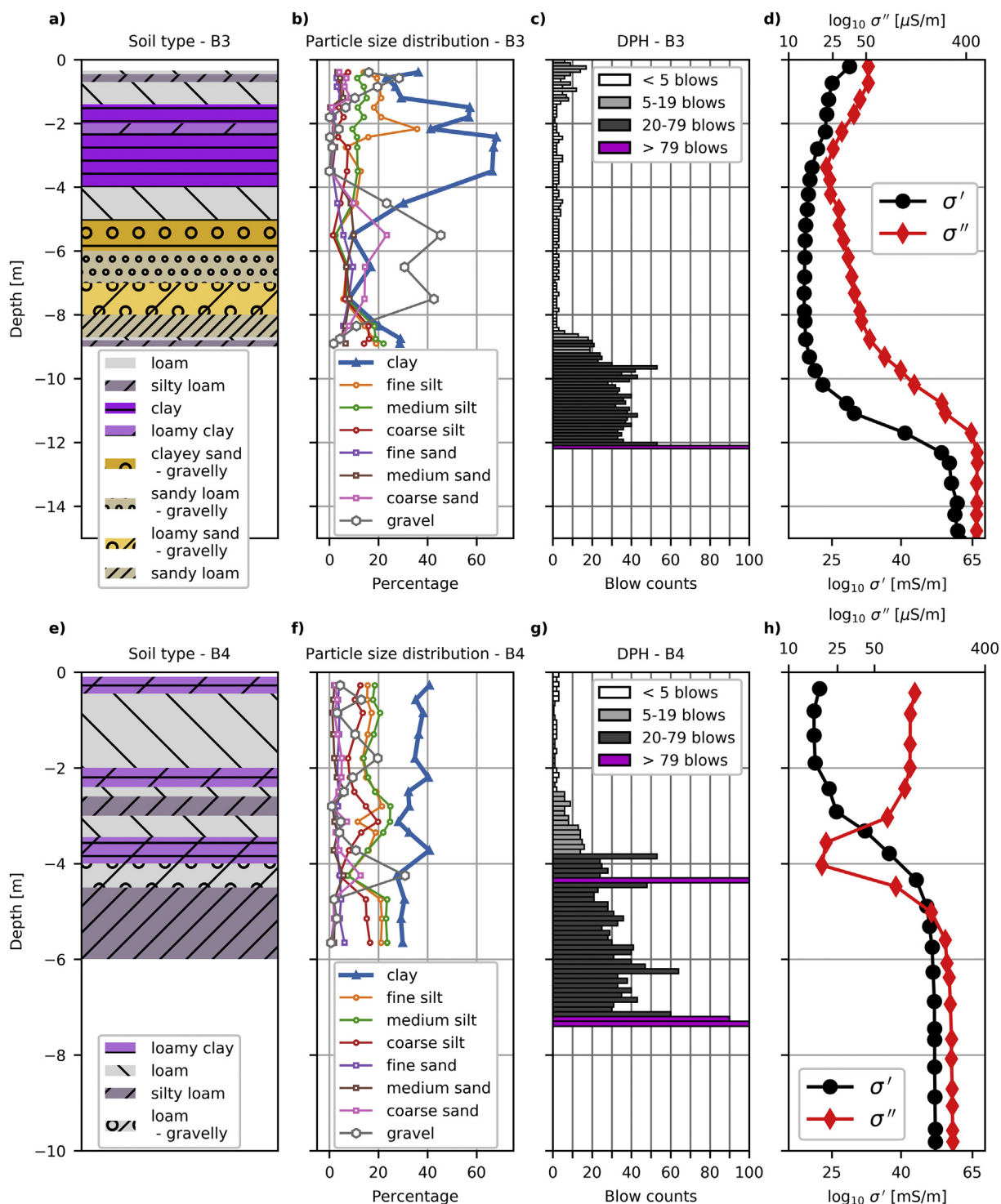


Fig. 5. Comparison of ground-truth and geophysical data: soil type (5a, 5e) and particle size distribution (5b, 5f) as obtained from the analysis of core drilling in B3 (5a, 5b) and B4 (5e, 5f); blow counts obtained from dynamic probing heavy (DPH) in the vicinity of B3 and B4 given in 10 cm increments (5c, 5g) and electrical parameters ( $\sigma'$  and  $\sigma''$ ) representing the median value from model parameters extracted from inverted profiles next to the wells (5d, 5h).

conductivity variations at depth for a given point and its correlation with ground-truth data is assessed prior to the presentation of the IP imaging results. Fig. 5 presents relevant textural and geotechnical parameters, namely, the soil type (Fig. 5a, e) and particle size distribution (Fig. 5b, f) as obtained from the analysis of core drillings, as well as the blow counts from co-located DPH surveys (Fig. 5c, g) for the wells B3 (Fig. 5a-5c) and B4 (Fig. 5e-5g), as well as the electrical model parameters expressed in terms of  $\sigma'$  and  $\sigma''$  (Fig. 5d, h) extracted from IP

imaging results (at 1 Hz) in the vicinity of wells B3 and B4.

The comparison of particle size distribution and the electrical properties shows the sensitivity of  $\sigma''$  to variations in the textural composition. In particular for B3, Fig. 5 shows that an increase in clay content (> 40%) is related to a significant decrease in the polarization effect (from 50 to 25  $\mu\text{S}/\text{m}$ ), as observed at depths between 2 and 4 m. For lower clay fractions (< 20%) and increasing the content of gravel and coarse sands (e.g., between 4 and 9 m depth),  $\sigma''$  increases, whereas

the increase appears to be correlated with the silt fractions that reveal an increase over the same depth range. Below 9 m depth, where no textural information is available,  $\sigma''$  continues to increase and reaches its maximum value ( $\sim 500 \mu\text{S/m}$ ) at 12 m depth. Such maximum correlates with high blow counts ( $> 79$  blows) and likely indicates the transition to un-weathered bedrock.

The  $\sigma'$  profile reveals only minor changes down to 9 m. There is a decrease in conductivity values from  $\sim 25 \text{ mS/m}$  between 1 and 3 m depth to  $\sim 10 \text{ mS/m}$  between 3 and 10 m, clearly indicating a poor sensitivity to textural variations. Nevertheless, the profile shows an increase in  $\sigma'$  values to the maximum value of  $60 \text{ mS/m}$  (Fig. 5d) at 12 m depth, which is in agreement with the increase in blow counts as previously discussed. Furthermore, Fig. 5 clearly reveals no correlation between the blow counts and the changes in the textural parameters in this core. For instance, the shallow soil samples (between 1 and 4 m depth) associated with the highest clay content ( $> 40\%$ ), and the deeper recovered materials (between 4 and 9 m depth) associated with coarser materials (gravels  $> 20\%$  and  $\sim 12.5\%$  clays), do not reveal any significant changes in the number of blow counts in DPH. This might be related to an unevenly distributed soil moisture in depth and needs further investigations.

The variations in  $\sigma''$  and textural parameters observed in well B4 (Fig. 5f, h) are consistent to those described above for B3: a decrease in the polarization effect for soils dominated by clay (e.g. from 60 to  $15 \mu\text{S/m}$  between 3 and  $\sim 4$  m depth) and an increase in  $\sigma''$  with increasing the gravel, sand and silt content. The observed increase in the polarization effect with increasing the content of coarse sediment is consistent with the recent developments in the understanding of the membrane polarization mechanism (e.g., Bückner and Hördt, 2013; Hördt et al., 2017). Such studies have demonstrated that an important parameter controlling the membrane polarization for a homogenous mineral composition is the contact between micro- and macropores, as well as the ratio between the pore-radii and pore-lengths. Furthermore, Chuprinko and Titov (2017) recently demonstrated that variations in the mineral composition of the different pores can also result in a polarization effect superimposing the polarization effect due to the pore-space geometry. Thus, we hypothesize that the observed increase in  $\sigma''$  is consistent with the contact of macropores in the coarse materials, and the micropores due to the fine grains. Accordingly, the  $\sigma''$  decreases in horizons dominated by fine silts and clays, where micropores dominate, and most of the energy is conducted along the mineral surface, thus, also explaining the relative high  $\sigma'$  values in the landslide.

The observed correlation between the textural, geotechnical and electrical parameters demonstrates that variations in  $\sigma'$  and  $\sigma''$  (at 1 Hz) can be used to delineate areas rich in fine-grained minerals (associated to low  $\sigma''$  at 1 Hz), which may also act as low hydraulic permeable layer hindering the infiltration of surface water. Consequently, high  $\sigma''$  values may indicate soils with variations of fine and coarse grains which may facilitate groundwater flow and act as drainage systems in the landslide.

#### 4.3.2. SIP imaging

We present in Fig. 6a the SIP imaging results for data collected along gr16 at three representative frequencies to investigate the frequency dependence of the electrical properties and its correlation with ground-truth data. As observed in Fig. 6a, the electrical conductivity ( $\sigma'$ ) reveals a negligible frequency dependence (in the frequency bandwidth analysed in this study) and will not be further addressed here. Textural analyses of sediments recovered after the drilling in B1 (Fig. 6b) and B2 (Fig. 6e) are shown to better investigate the control of the spectral response (i.e., the frequency dependence) of  $\sigma''$ . Moreover, Fig. 6 shows the DPH soundings conducted in the vicinity of the wells B1 (Fig. 6c) and B2 (Fig. 6f). Fig. 6d and g presents the spectral amplitude, i.e.  $\sigma''$ , as a function of depth and frequency. The  $\sigma''$  values were extracted from the electrical images after independent inversion of data collected at each frequency. In general the analysis of soil samples revealed high

fractions of fine-grained minerals: clay (20–50%) and silt (10–25%) and low contents of coarser grains (sand and gravel roughly  $< 10\%$ ). The abundance of fine grains is consistent with the relatively modest  $\sigma''$  response in the low frequencies ( $< 15$  Hz); yet a linear increase in the  $\sigma''$  values can be observed with increasing the frequency. Such increase in the polarization effect with increasing the frequency is related to the fastest polarization processes in fine grains, where the ions move along shorter trajectories, as observed previously in laboratory studies conducted in clay-rich samples (e.g., Slater and Lesmes, 2002; Slater et al., 2006; Jougnot et al., 2010). The increase at high frequencies is nevertheless only visible in the saturated materials (below 2 m depth), as pore water is necessary for the development of the electrical double layer where the polarization takes place. The increased  $\sigma''$  response for B2 between 0 and 1.5 m might be a result of a separated fully saturated patch, as for instance expected for the waterlogged areas. The unsaturated zone is also interpreted as weak materials following the DPH ( $< 5$  blows), with an increase in the DPH counts also observed below 2 m depth.

We observe a noticeable change of  $\sigma''$  below 6 m depth for B1 and below 9 m depth for B2, at depths where no textural information is available. In particular, plots in Fig. 6d reveal (i) an overall increase in  $\sigma''$  for frequencies  $> \sim 1.66$  Hz and (ii) a noticeable peak for  $\sigma''$  with values well above  $700 \mu\text{S/m}$ . Such peak is situated in the frequency range of 7.5–15 Hz and appears to shift towards lower frequencies with increasing depth, indicating a change in the dominating length scale towards coarser grains (medium to coarse silts), i.e., and slower polarization processes. The DPH also reveals an increase in the material strength below 6 m depth for B1 and below 9 m depth for B2 ( $> 40$  blows). Furthermore, the shift of the  $\sigma''$  peak to even lower frequencies at 9 m depth for B1 and 11 m depth for B2 is also accompanied by a transition to blow counts above 79 and likely indicates the contact to un-weathered bedrock and larger length-scales dominating the polarization response. Hence, it appears that analysis of the frequency dependence of the polarization effect could be used to distinguish contacts between materials with different mechanical properties.

Nevertheless, analysis of high frequency IP data for field measurements needs to be performed with caution, considering that increasing the frequency ( $> 10$  Hz) also leads to the induction of parasitic electromagnetic fields that contaminate the SIP data (Flores Orozco et al., 2013). Commonly referred to as electromagnetic coupling (EM-coupling), it arises due to current flow along the cables connecting the instrument and the electrodes, due to differences in the contact between electrodes and the ground, and due to self-induction effects between the cables (e.g., Zimmermann et al., 2008; Flores Orozco et al., 2013). It is proportional to the  $\sigma'$  and the square of the excitation frequency (Dey and Morrison, 1973). In case of clay-rich minerals, EM-coupling might superimpose the actual response from the subsurface; thus, in Fig. 6f we do not present data collected at higher frequencies ( $> 100$  Hz), as such data revealed EM-coupling.

#### 4.4. IP mapping

Fig. 7 presents the IP imaging results for the profile gr5 expressed in terms of  $\sigma'$  and  $\sigma''$ , with the related geomorphological features, groundwater levels and blow counts measured by DPH superimposed over the electrical images. The imaging results reveal two main units: (i) a top layer characterized by low  $\sigma'$  ( $< 30 \text{ mS/m}$ ) and  $\sigma''$  ( $< 150 \mu\text{S/m}$ ) values, with a varying thickness along the profile, and (ii) a deeper unit associated to high spatial variability and a broader range in the  $\sigma'$  and  $\sigma''$  values. We observe a significant decrease in thickness of the  $\sigma'$  top layer from 12 m to  $\sim 4$  m at the location of the top-scarp. From the position of the top-scarp ( $\sim 48$  m), the vertical contact observed in the  $\sigma'$  image from low to intermediate ( $> 30 \text{ mS/m}$ )  $\sigma'$  values is consistent to the vertical contact interpreted from DPH (Canli et al., under revision), interpreted as the location of the sliding plane, as depicted in Fig. 7. Moreover, the  $\sigma'$  contact observed at larger depth ( $> 12$  m below

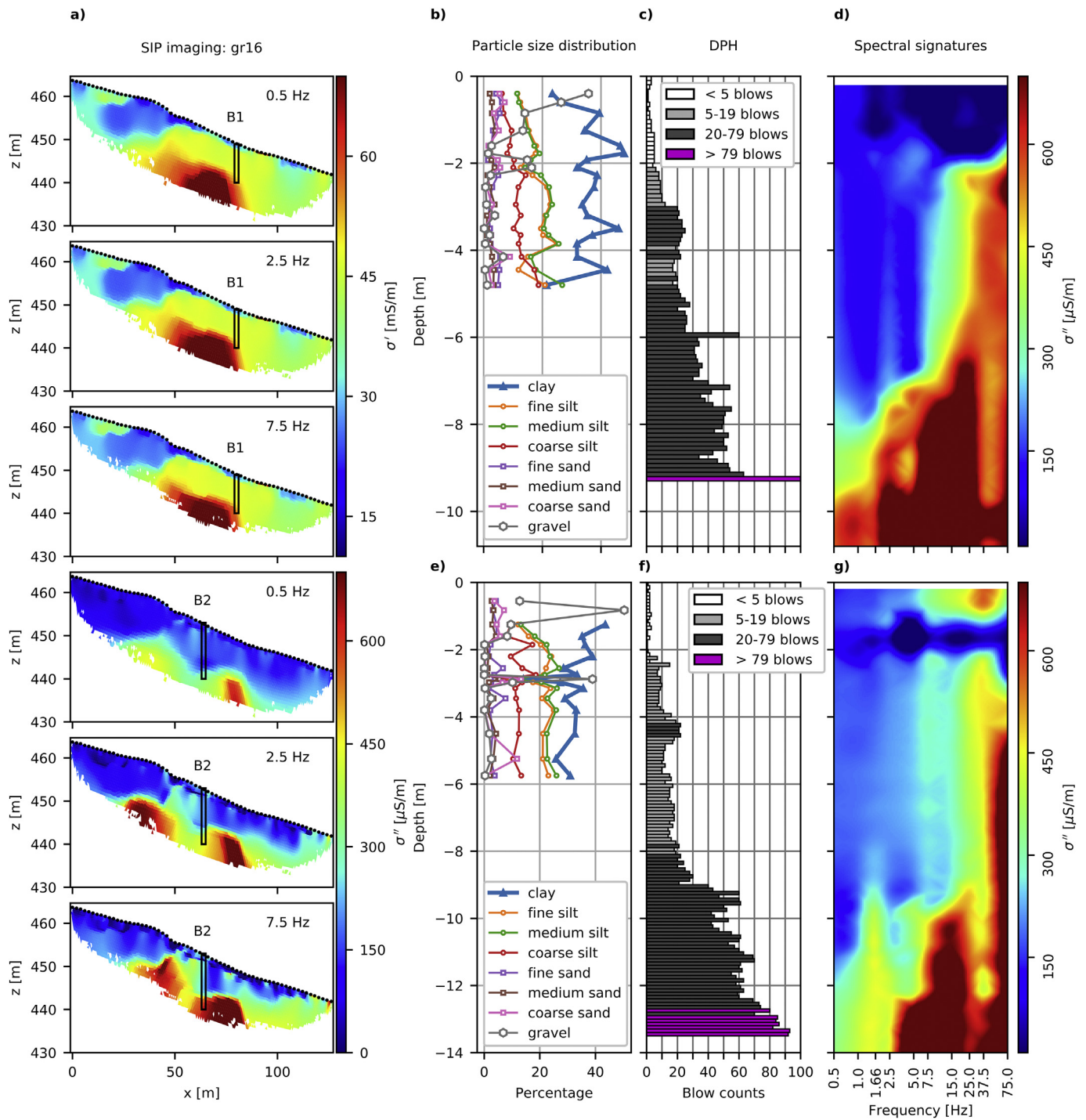


**Fig. 6.** Comparison of ground-truth and geophysical data. SIP imaging results ( $\sigma'$ ,  $\sigma''$ ) for the frequencies of 0.5, 2.5, and 7.5 Hz to investigate the frequency dependence of the polarization effect (6a). Particle size distribution as obtained from the analysis of core drilling at B1 (6b) and B2 (6e) and blow counts from dynamic probing heavy (DPH) in the vicinity of B1 (6c) and B2 (6f) given in 10 cm increments. Spectral amplitudes ( $\sigma''$ ) as a function of depth and frequency as extracted from the imaging results of gr16 (6d, 6g).

ground surface), associated to a transition to the highest  $\sigma'$  values ( $> 70$  mS/m), is in agreement with highest blow counts ( $> 79$  blows) in the DPH and likely suggest the contact to bedrock consisting of sedimentary rocks (mottled marls or Flysch materials, e.g., sandstone). Furthermore, only a poor correlation of variations in  $\sigma'$  with the groundwater levels can be observed, which indicates that surface conduction mechanisms (due to overall high clay content) dominate over ionic conduction (through water-filled pores).

Imaging results for the polarization effect ( $\sigma''$ ) reveal higher spatial

variability than those for  $\sigma'$ , in particular for the unit below the sliding plane (as interpreted from the  $\sigma'$  image). In the stable material, lateral variations in  $\sigma''$  values range between 150 and 550  $\mu\text{S/m}$  suggesting differences in soil properties. In particular, in Fig. 7, we observe an anomaly in the highly polarizable layer ( $> 500$   $\mu\text{S/m}$ ) at  $\sim 12$  m depth, between 45 and 65 m along the profile, which roughly corresponds with the position of the top and central-scarp. We interpret this discontinuity as a transition from marlstone or sandstones ( $\sigma' < 60$  mS/m,  $\sigma'' > 400$   $\mu\text{S/m}$ ) to fractured marlstone ( $\sigma' > 60$  mS/m,  $\sigma'' \sim 300$   $\mu\text{S/m}$ ).

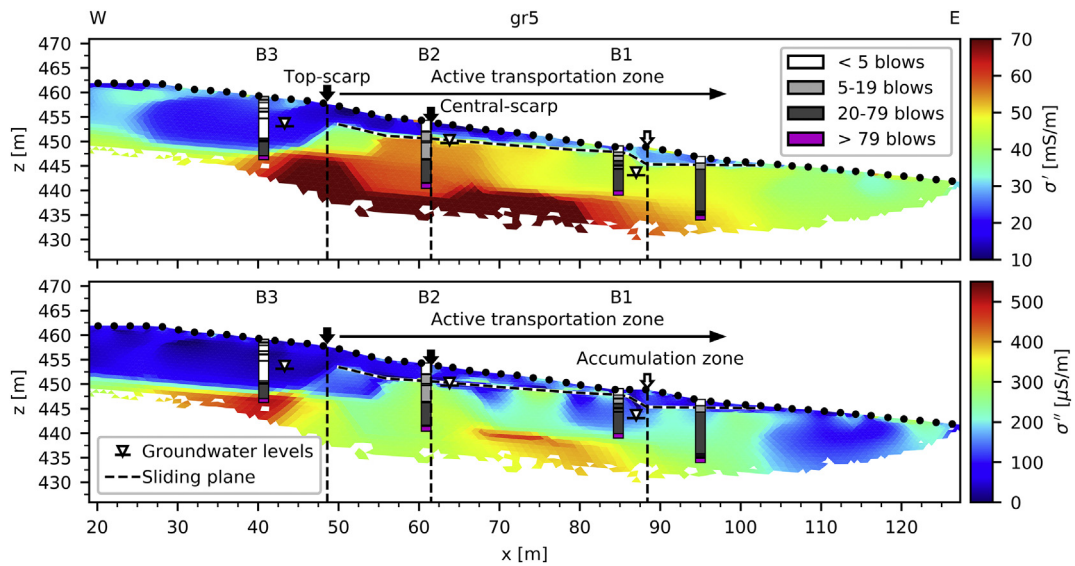


Fig. 7. Imaging results expressed in terms of the real (top) and imaginary (bottom) components of the complex electrical conductivity. The blow counts measured by DPH, the groundwater levels, as well as geomorphological features, namely the landslide scarps, the accumulation zone and active transportation zone are superimposed over the electrical images.

However, the lack of deep core-drillings impedes a quantitative interpretation of the electrical properties at depth. Subsurface materials between the sliding plane and the layer at depth can be interpreted as variably weathered marlstones or Flysch materials. Considering the high variability in  $\sigma'$  and  $\sigma''$  values, areas associated to different stages of weathering can be outlined.

As discussed earlier, variations in  $\sigma''$  values are associated with changes in clay content and not compaction, therefore variations in  $\sigma''$  values do not necessarily need to trace the increase in blow counts observed in the DPH data. The assessment of clay-rich zones in landslides is of high relevance, as those may represent important variations in the subsurface hydraulic properties, with such clays commonly related to zones of low hydraulic permeability (e.g., Slater and Lesmes, 2002). Thus, spatial characterization of clay-rich zones is critical for the delineation of interflow or groundwater flow paths and, thus, a better understanding of possible triggering mechanisms. Based on the interpretation of single-frequency and SIP signatures discussed above, imaging results presented in Fig. 7 reveal a zone of low hydraulic conductivity, characterized by low  $\sigma''$  ( $< 200 \mu\text{S}/\text{m}$ ) and intermediate  $\sigma'$  ( $\sim 40 \text{ mS}/\text{m}$ ) values, between 45 and 55 m along profile direction. Consistently, this particular area corresponds with the location of the top-scarp and the start of the shallow sliding plane, defined by geomorphological surveying and geotechnical data. Hence, it is possible to suggest that such area may act as a hydraulic barrier retaining groundwater and promoting the built-up of positive pore-water pressure, thus, facilitating the mobilization of the materials due to the reduction of shear strength. In a similar way, the shallow  $\sigma''$  anomaly observed between 75 and 85 m (along profile direction) may also indicate an area of low hydraulic conductivity, hindering the percolation of surface water; thus, resulting in the waterlogged zone defined during the geomorphological mapping. Hence, variability in  $\sigma''$  solved in the imaging results seems to be well correlated with changes in the hydraulic properties of the subsurface, as evidenced by the geomorphological features of the landslide.

Furthermore, Fig. 8 presents the imaging results for three WE profiles which are representative for the northern (gr3), the central (gr5) and the southern (gr9) regions of the landslide. Consistently to gr5, IP imaging results reveal the existence of two main units: a top layer characterized by low  $\sigma'$  ( $< 30 \text{ mS}/\text{m}$ ) and  $\sigma''$  ( $< 150 \mu\text{S}/\text{m}$ ) values, on top of a more conductive unit ( $> 45 \text{ mS}/\text{m}$ ) associated to high spatial variability in  $\sigma''$ . The observed decrease in the  $\sigma'$  top layer at the location

of the top-scarp for gr5 is consistently resolved for all profiles and again indicates the transition to the active landslide body. Consistently, the deep  $\sigma''$  anomaly, located between the top and central-scarp, can also be observed in plots for gr3 and gr6, and to certain extent also gr9. Such anomaly, as discussed before, is most probably related to different stages of weathering and therefore zones of contrasting hydraulic properties; thus, of high relevance for the understanding of water flow within the landslide.

#### 4.5. Interpretation of the landslide

Maps of the  $\sigma_a$  obtained from EMI mapping reveal clear units consistent with geomorphological characteristics of the landslide, namely, the top and central-scarp, as well as with the accumulation zone and the waterlogged areas. However, due to the nature of the EMI measurements representing a non-linear average over a specific depth range, no information on the depths of the delineated structures can be provided. Yet, the discussion of the IP imaging results presented earlier has demonstrated that the changes in the electrical properties are well correlated with the different ground-truth data (e.g., grain size analysis, DPH). Therefore, we present in Fig. 9 interpolated maps of the  $\sigma'$  and  $\sigma''$  for different depths (1–1.5 m, 2.5–3 m, 5–5.5 m, 8.5–9 m, 10.5–11 m) as obtained from the inversion of the entire data sets (gr1 to gr16) at 1 Hz, superimposing the geomorphological information (landslide scarps and accumulation zone). High  $\sigma'$  and  $\sigma''$  ( $> 60 \text{ mS}/\text{m}$ ,  $> 500 \mu\text{S}/\text{m}$ ) values observed at the northern part of the landslide are the effect of anthropogenic structures (e.g., power line cables) and will not be further discussed here.

Plots presented in Fig. 9a reveal that for shallow depths the highest  $\sigma'$  values are located mainly at the foot of the landslide (i.e., to the east of the accumulation zone). With depth, an increase in  $\sigma'$  (from  $\sim 20$  to  $70 \text{ mS}/\text{m}$ ) values can be observed for the eastern region of the landslide, which is accompanied by a transition of the conductive anomaly towards the center of the study site (Fig. 9b–9i). Images of the polarization effect (Fig. 9b–9j) show similarities to those obtained for  $\sigma'$ , yet maps of the polarization effect are characterized by a higher spatial variability (e.g., Fig. 9j). The top-scarp (located at the topographical highest area of the landslide) shows a stronger correlation with the contacts in the electrical properties for deep maps (Fig. 9g–9j). In the case of the central-scarp, its geomorphological features appear to be better resolved for  $\sigma'$  maps constructed at intermediate depths (Fig. 9c–

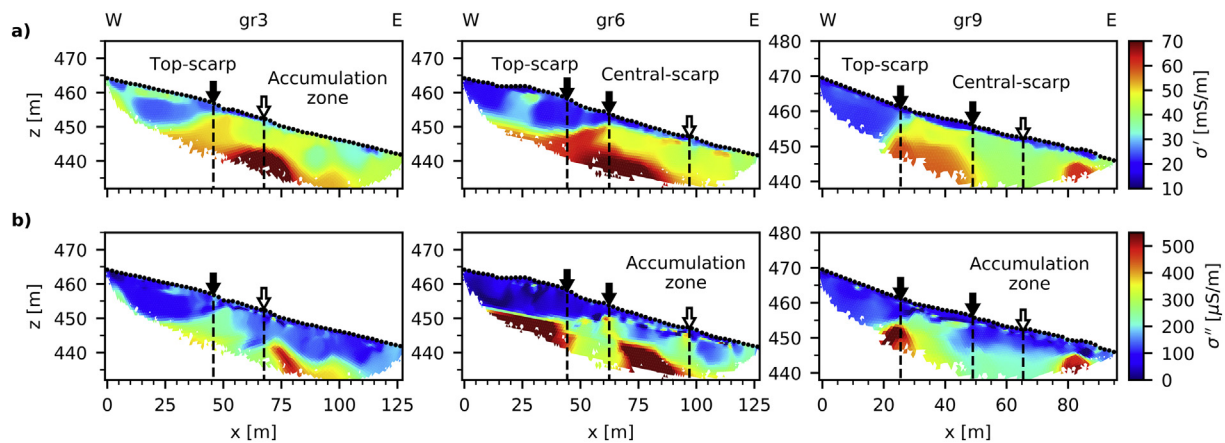


**Fig. 8.** Imaging results for three WE profiles in terms of the real (8a) and imaginary (8b) components of the complex electrical conductivity. The geomorphological features (top-scarp, central-scarp and accumulation zone) are indicated by surface arrows.

9f) and for  $\sigma''$  maps for intermediate and large depths (Fig. 9f, h, j), demonstrating that  $\sigma''$  patterns do not necessarily mirror the patterns observed for  $\sigma'$ .

Maps of the electrical properties further reveal that areas located above the top-scarp are characterized by the lowest  $\sigma'$  and  $\sigma''$  ( $< 10$  mS/m,  $< 100$   $\mu$ S/m) values, and therefore can be associated to clay-rich zones. Such low permeable zones reduce the infiltration of surface water and foster surface run-off towards the active transportation zone (below the top-scarp). The excess of surface water in the respective area will lead to more water in the lower reaches, where it can infiltrate in the soil and further increase the soil moisture of the already weakened sliding material. The increase in soil moisture is a well-known triggering mechanism for shallow landslides and has been often investigated (e.g. van Asch et al., 1999). Furthermore, the topographical bulge at the accumulation zone leads to the development of a surface pan, additionally accumulating the surface water and enhancing its infiltration into the ground. In a similar way, interflow and groundwater flowing down-gradient from the hilltop will reach a poorly permeable subsurface zone between the top and central scarp characterized by low  $\sigma''$  ( $< 100$   $\mu$ S/m) values as discussed in a previous section (e.g. Fig. 9b, d, f). In this respective area, groundwater and soil water retention will occur, which in turn can promote a built-up of positive pore-water pressure and the reduction in shear-strength. Hence, possible remediation actions might include the removal of the flat surface pan and the installation of a drainage system.

Plots presented in Fig. 9 also demonstrate that there seems to be no significant change in the conductivity and polarization patterns explaining the accumulation zone. This might be a result of the spatial dimension of such zone, with a west-east extension in the order of magnitude of the electrode spacing (2 m). Hence, the accumulation zone might not be resolved with the conducted IP surveys; yet it is properly delineated through the EMI mapping. When comparing the  $\sigma_{6.7}$  maps (c.f. Fig. 3c) with the shallow interpolated  $\sigma'$  maps (Fig. 9a, c), we observe a close similarity in the patterns of  $\sigma_a$  and  $\sigma'$ . Moreover, such depth between 1 and 3 m represents the expected location of the sliding plane as obtained from geotechnical investigations (Canli et al., under revision). Thus, the changes observed in the conductivity patterns in Fig. 9a and c, i.e. an increase in  $\sigma'$  (from 25 to 50 mS/m) values particularly for the area below the central scarp, validates the interpretation made earlier for the EMI maps regarding the contact to the sliding plane.

Fig. 10 shows the conceptual model of the landslide as derived from a joint interpretation of geophysical, hydrogeological, geomorphological and geotechnical data. The plot presents the different interpreted soil types and hydrogeological units and their geophysical indicators ( $\sigma'$ ,  $\sigma''$ ), the location of the sliding plane, as well as the corresponding

groundwater flow paths. In particular, four types of run-off were interpreted: 1) groundwater flow through strongly weathered sedimentary materials above the top-scarp (black arrows in Fig. 10), 2) seepage and retarded groundwater flow through variably weathered marlstone as delineated by spatial variations in  $\sigma'$  and  $\sigma''$  below the sliding plane (red arrows in Fig. 10), 3) interflow within the mobilized material and along the sliding plane, and 4) surface run-off due to high clay content. Fig. 10 clearly demonstrates the benefit of using multiple geophysical, hydrogeological, geomorphological and geotechnical methods for landslide characterization.

## 5. Conclusion

In this study, we have presented the joint application of the EMI and IP methods, and the corresponding interpretation of the mapping data for the characterization of a shallow, clay-rich landslide. Extensive geotechnical, geomorphological and hydrogeological data available at the study area allowed to evaluate the geophysical response and formulate a conclusive interpretation of the imaging results. Based on the EMI maps lateral changes in the electrical conductivity could be identified. The main patterns correlate well with geomorphological features, namely, with the main scarps, the accumulation zone and waterlogged areas, as well as preferential areas for the infiltration of surface water. The latter represents relevant information for the potential design of drainage systems. Moreover, IP imaging results were used to delineate the geometry of the sliding plane and the different soil types and hydrogeological units, which, in combination with the available information from a piezometric network, dynamic probing and grain size analyses in recovered drilling cores, permitted to delineate groundwater flow patterns. Additionally, information about the subsurface capacitive properties provided by the images of the polarization effect allowed to discriminate between materials of different textural composition. Furthermore, our SIP imaging results clearly revealed changes in the frequency dependence of the polarization effect associated to changes in the grain size. Such findings again correlate with geotechnical and soil textural data. The validation of our results using extensive ground-truth data clearly shows the suitability of combined EMI mapping and IP imaging methods for a better characterization and understanding of clay-rich landslides.

## Acknowledgements

This work is supported through the Austrian Science Fund (FWF) – Agence Nationale de la Recherche (ANR) research project I 2619-N29 and ANR-15-CE04-0009-01 HYDRO-SLIDE: Hydro-geophysical observations for an advanced understanding of clayey landslides, as well

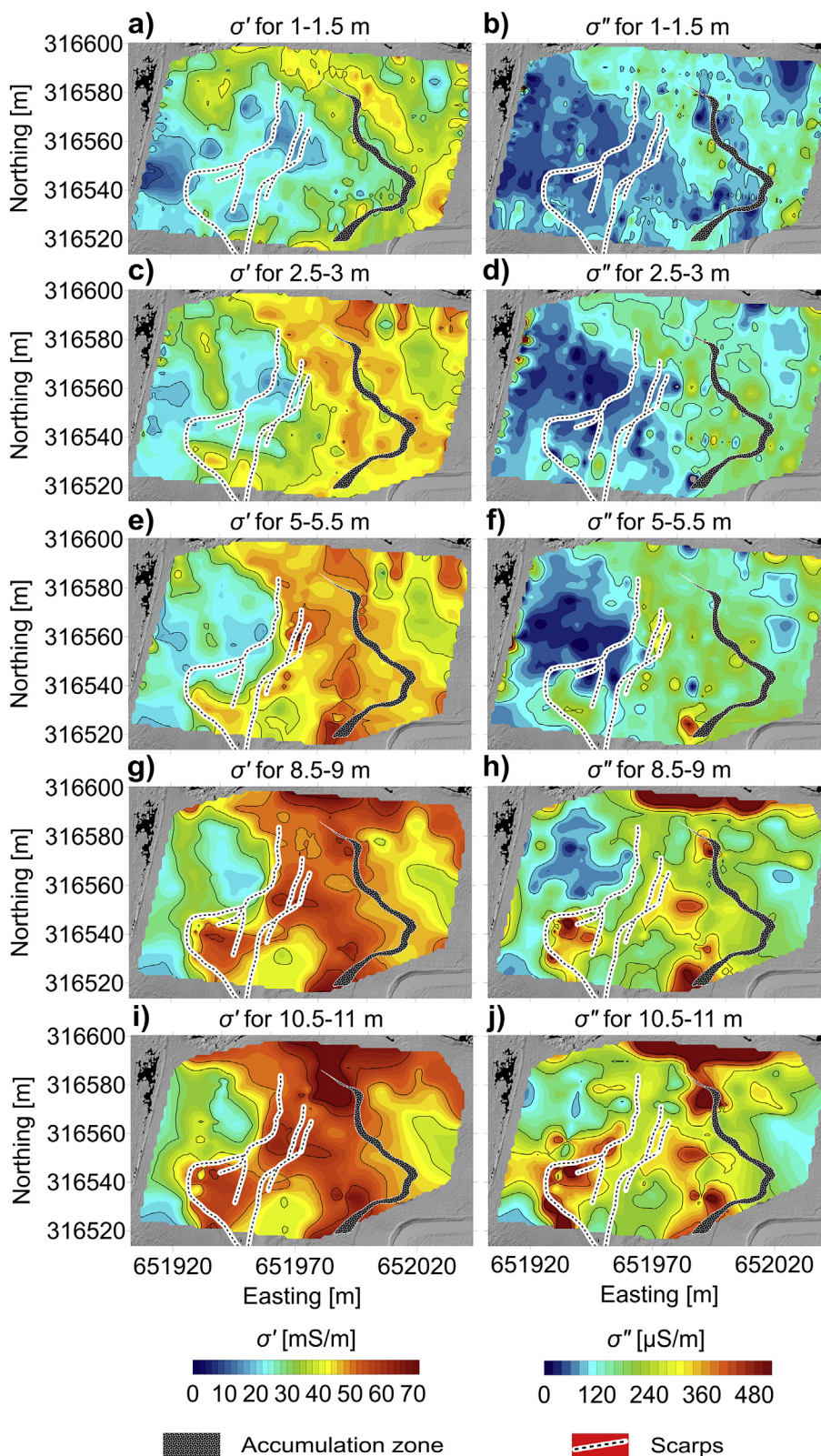
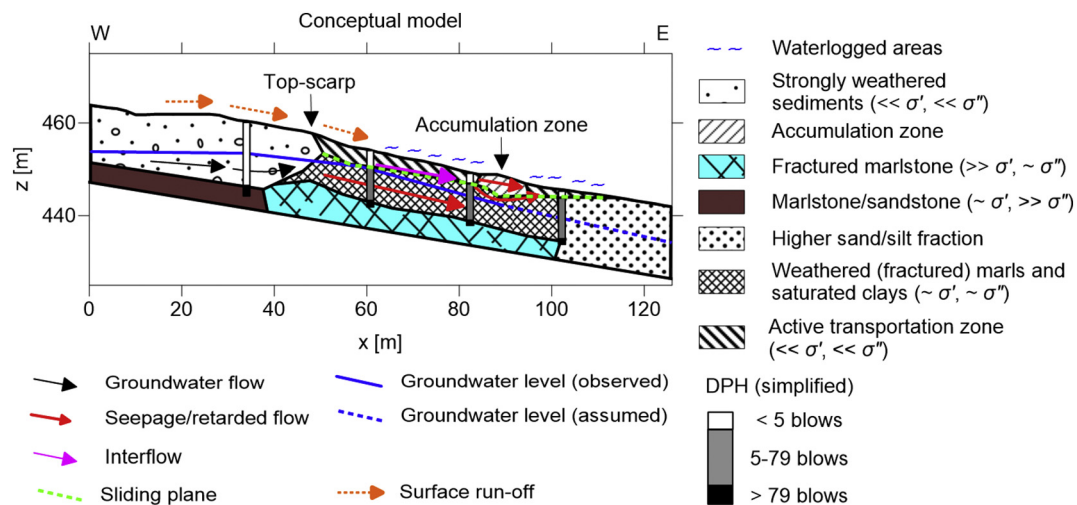


Fig. 9. Maps constructed for different depths based on the IP imaging results in terms of the real ( $\sigma'$  – 9a, 9c, 9e, 9g, 9i) and imaginary ( $\sigma''$  – 9b, 9d, 9f, 9h, 9j) components of the complex electrical conductivity.

as through the NoeSLIDE project: Monitoring of different landslide types in Lower Austria, which is kindly co-financed by the Geological Survey of the Federal State Government of Lower Austria. Furthermore, the University of Vienna provided additional funds for setting up the monitoring system. Aerial image and DEM provided by the Federal

State Government of Lower Austria. Thanks are also due to the municipality of Gresten, and indeed, to the landowner, who allows us to work on his property to further understand the landslide dynamics.



**Fig. 10.** Conceptual model of the landslide indicating the different soil types and hydrogeological units as derived from the joint interpretation of geophysical, hydrogeological, geomorphological and geotechnical data.

**References**

Aldorff, D., Dietrich, P., 2014. Delineation of areas with different temporal behavior of soil properties at a landslide affected Alpine hillside using time-lapse electromagnetic data. *Environ. Earth Sci.* 72 (5), 1357–1366. <https://doi.org/10.1007/s12665-014-3240-7>.

van Asch, T.W.J., Buma, J., Beek, van, 1999. A view on some hydrological triggering systems in landslides. *Geomorphology* 30 (1–2), 25–33. [https://doi.org/10.1016/S0169-555X\(99\)00042-2](https://doi.org/10.1016/S0169-555X(99)00042-2).

Bell, R., Kruse, J.-E., Garcia, A., Glade, T., 2006. Subsurface investigations of landslides using geophysical methods – geoelectrical applications in the Swabian Alb (Germany). *Geograph. Helv.* 61 (3), 201–208. <https://doi.org/10.5194/gh-61-201-2006>.

Binley, A., Kemna, A., 2005. DC Resistivity and Induced Polarization Methods, in: *Hydrogeophysics*. Water Science and Technology Library. Springer, Dordrecht, pp. 129–156. [https://doi.org/10.1007/1-4020-3102-5\\_5](https://doi.org/10.1007/1-4020-3102-5_5).

Binley, A., Slater, L., Fukes, M., Cassiani, G., 2005. The relationship between spectral induced polarization and hydraulic properties of saturated and unsaturated sandstone. *Water Resour. Res.* 41 (12). <https://doi.org/10.1029/2005WR004202>.

Binley, A., Hubbard, S.S., Huisman, J.A., Revil, A., Robinson, D.A., Singha, K., Slater, L.D., 2015. The emergence of hydrogeophysics for improved understanding of subsurface processes over multiple scales. *Water Resour. Res.* 51, 3837–3866. <https://doi.org/10.1002/2015WR017016>.

Blaschek, R., Hördt, A., Kemna, A., 2008. A new sensitivity-controlled focusing regularization scheme for the inversion of induced polarization data based on the minimum gradient support. *Geophysics* 73, F45–F54. <https://doi.org/10.1190/1.2824820>.

Brevik, E.C., Fenton, T.E., Lazari, A., 2006. Soil electrical conductivity as a function of soil water content and implications for soil mapping. *Precis. Agric.* 7, 393–404. <https://doi.org/10.1007/s11119-006-9021-x>.

Bücker, M., Hördt, A., 2013. Long and short narrow pore models for membrane polarization. *Geophysics* 78, E299–E314. <https://doi.org/10.1190/geo2012-0548.1>.

Callegary, J.B., Ferré, T.P.A., Groom, R.W., 2007. Vertical Spatial Sensitivity and Exploration Depth of Low-Induction-Number Electromagnetic-Induction Instruments. *Vadose Zone J.* 6, 158–167. <https://doi.org/10.2136/vzj2006.0120>.

Campbell, R.H., 1975. *Soil Slips, Debris Flows, and Rainstorms in the Santa Monica Mountains and Vicinity, Southern California (USGS Numbered Series no. 851)*, Professional Paper. Govt. Print. Off, U.S.

Canli, E., Engels, A., Thiebes, B., Groiss, B., Glade, T., Schweigl, J., Bertagnoli, M., Under revision. Evaluating landslide dynamics and internal structure – a case study from the Salcher landslide observatory, Austria-Bull. Eng. Geol. Environ.

Chuprinko, Daniil, Titov, Konstantin, 2017. Influence of mineral composition on spectral induced polarization in sediments. *Geophys. J. Int.* 209 (1), 186–191. <https://doi.org/10.1093/gji/ggx018>. (1 April).

Cosenza, P., Marmet, E., Rejiba, F., Cui, Y.J., Tabbagh, A., Charley, Y., 2006. Correlations between geotechnical and electrical data: a case study at Garchy in France. *J. Appl. Geophys.* 60 (3–4), 165–178. <https://doi.org/10.1016/j.jappgeo.2006.02.003>.

Dahlin, T., Löfroth, H., Schälin, D., Suer, P., 2013. Mapping of quick clay using geoelectrical imaging and CPTU-resistivity. *Near Surf. Geophys.* 11 (6), 659–670.

Dey, A., Morrison, H.F., 1973. Electromagnetic coupling in frequency and time-domain induced-polarization surveys over a multilayered earth. *Geophysics* 38 (2), 380–405. <https://doi.org/10.1190/1.1440348>.

Doetsch, J., Ingeman-Nielsen, T., Christiansen, A.V., Fiandaca, G., Auken, E., Elberling, B., 2015. Direct current (DC) resistivity and induced polarization (IP) monitoring of active layer dynamics at high temporal resolution. *Cold Reg. Sci. Technol.* 119, 16–28. <https://doi.org/10.1016/j.coldregions.2015.07.002>.

Doolittle, J.A., Brevik, E.C., 2014. The use of electromagnetic induction techniques in soils studies. *Geoderma* 223–225, 33–45. <https://doi.org/10.1016/j.geoderma.2014.01.027>.

Everett, M.E., 2005. What do electromagnetic induction responses measure? *Lead. Edge* 24 (2), 154–157. <https://doi.org/10.1190/1.1876038>.

Everett, M.E., 2012. Theoretical developments in electromagnetic induction geophysics with selected applications in the near surface. *Surv. Geophys.* 33 (1), 29–63. <https://doi.org/10.1007/s10712-011-9138-y>.

Flores Orozco, A., Williams, K.H., Long, P.E., Hubbard, S.S., Kemna, A., 2011. Using complex resistivity imaging to infer biogeochemical processes associated with bioremediation of an uranium-contaminated aquifer. *J. Geophys. Res. Biogeosci.* 116. <https://doi.org/10.1029/2010JG001591>. G03001.

Flores Orozco, A., Kemna, A., Zimmermann, E., 2012a. Data error quantification in spectral induced polarization imaging. *Geophysics* 77 (3), E227–E237.

Flores Orozco, A., Kemna, A., Oberdörster, C., Zschornack, L., Leven, C., Dietrich, P., Weiss, H., 2012b. Delineation of subsurface hydrocarbon contamination at a former hydrogenation plant using spectral induced polarization imaging. *J. Contam. Hydrol.* 136, 131–144. <https://doi.org/10.1016/j.jconhyd.2012.06.001>.

Flores Orozco, A., Williams, K.H., Kemna, A., 2013. Time-lapse spectral induced polarization imaging of stimulated uranium bioremediation. *Near Surface Geophysics* 11, 531–544. <https://doi.org/10.3997/1873-0604.2013020>.

Flores Orozco, A., Velimirovic, M., Tosco, T., Kemna, A., Sapion, H., Klaas, N., Sethi, R., Bastiaens, L., 2015. Monitoring the Injection of Microscale Zerovalent Iron Particles for Groundwater Remediation by Means of complex Electrical Conductivity Imaging. *Environ. Sci. Technol.* 49 (9), 5593–5600. <https://doi.org/10.1021/acs.est.5b00208>.

Flores Orozco, A., Gallistl, J., Bücker, M., Williams, K.H., 2018. Decay curve analysis for data error quantification in time-domain induced polarization imaging. *Geophysics* 83 (2), E75–E86. <https://doi.org/10.1190/geo2016-0714.1>.

Fressard, M., Maquaire, O., Thiery, Y., Davidson, R., Lissak, C., 2016. Multi-method characterization of an active landslide: Case study in the Pays d’Auge plateau (Normandy, France). *Geomorphology* 270, 22–39. <https://doi.org/10.1016/j.geomorph.2016.07.001>.

Glade, T., Kadereit, A., Dikau, R., 2001. Landslides at the Tertiary Escarpments of Rheinhessen, Germany. *Zeitschrift für Geomorphologie Suppl.* Vol. 125. pp. 65–92.

Glade, T., Stark, P., Dikau, R., 2005. Determination of potential landslide shear plane depth using seismic refraction — a case study in Rheinhessen, Germany. *Bull. Eng. Geol. Environ.* 64 (2), 151–158. <https://doi.org/10.1007/s10064-004-0258-1>.

Gottschling, P., 2006. Massenbewegungen. In: Wessely, G., Draxler, I., Gangl, G., Gottschling, P., Heinrich, M., Hofmann, T., Lenhardt, W., Matura, A., Pavuza, R., Peresson, H., Sauer, R. (Eds.), *Geologie der österreichischen Bundesländer - Niederösterreich*. Geologische Bundesanstalt, Wien, pp. 335–340.

Grandjean, G., Gourry, J.C., Sanchez, O., Bitri, A., Garambois, S., 2011. Structural study of the Ballandaz landslide (French Alps) using geophysical imagery. *J. Appl. Geophys.* 75 (3), 531–542. <https://doi.org/10.1016/j.jappgeo.2011.07.008>.

Hack, R., 2000. Geophysics for slope stability. *Surv. Geophys.* 21, 423–448. <https://doi.org/10.1023/A:1006797126800>.

von Hebel, C., Rudolph, S., Mester, A., Huisman, J.A., Kumbhar, P., Vereecken, H., van der Kruk, J., 2014. Three-dimensional imaging of subsurface structural patterns using quantitative large-scale multiconfiguration electromagnetic induction data. *Water Resour. Res.* 50 (3), 2732–2748. <https://doi.org/10.1002/2013WR014864>.

Hördt, A., Bairlein, K., Bielefeld, A., Bücker, M., Kuhn, E., Nordsiek, S., Stebner, H., 2016. The dependence of induced polarization on fluid salinity and pH, studied with an extended model of membrane polarization. *J. Appl. Geophys.* 135, 408–417. <https://doi.org/10.1016/j.jappgeo.2016.02.007>.

Hördt, A., Bairlein, K., Bücker, M., Stebner, H., 2017. Geometrical constraints for membrane polarization. *Near Surface Geophysics* 15 (6), 579–592. <https://doi.org/10.3997/1873-0604.2017053>.

Jongmans, D., Garambois, S., 2007. Geophysical investigation of landslides: a review. *Bull. Soc. Géol. France* 178 (2), 101–112. <https://doi.org/10.2113/gssgbull.178.2.101>.

- Jougnot, D., Ghorbani, A., Revil, A., Leroy, P., Cosenza, P., 2010. Spectral induced polarization of partially saturated clay-rocks: a mechanistic approach. *Geophys. J. Int.* 180 (1), 210–224. <https://doi.org/10.1111/j.1365-246X.2009.04426.x>.
- Keller, G.V., Frischknecht, F.C., 1966. *Electrical Methods in Geophysical Prospecting*. Kemna, A., 2000. *Tomographic Inversion of Complex Resistivity: Theory and Application*. Der Andere Verlag Osnabrück, Germany.
- Kemna, A., Vanderborght, J., Kulesha, B., Vereecken, H., 2002. Imaging and characterisation of subsurface solute transport using electrical resistivity tomography (ERT) and equivalent transport models. *J. Hydrol.* 267 (3–4), 125–146. [https://doi.org/10.1016/S0022-1694\(02\)00145-2](https://doi.org/10.1016/S0022-1694(02)00145-2).
- Kemna, A., Binley, A., Slater, L., 2004. Crosshole IP imaging for engineering and environmental applications. *Geophysics* 69, 97–107. <https://doi.org/10.1190/1.1649379>.
- Kemna, A., Binley, A., Cassiani, G., Niederleithinger, E., Revil, A., Slater, L., Williams, K.H., Orozco, A.F., Haegel, F.-H., Hoerd, A., Kruschwitz, S., Leroux, S., Titov, K., Zimmermann, E., 2012. An overview of the spectral induced polarization method for near-surface applications. *Near Surface Geophysics* 10 (6), 453–468. <https://doi.org/10.3997/1873-0604.2012027>.
- Kušnirák, D., Dostál, I., Putiška, R., Mojež, A., 2016. Complex geophysical investigation of the Kapušany landslide (Eastern Slovakia). *Contrib. Geophys. Geodesy* 46, 111–124. <https://doi.org/10.1515/congeo-2016-0008>.
- Labrecque, D.J., Daily, W., 2008. Assessment of measurement errors for galvanic-resistivity electrodes of different composition. *Geophysics* 73 (2), F55–F64. <https://doi.org/10.1190/1.2823457>.
- Labrecque, D.J., Ward, S.H., 1990. Two dimensional cross-borehole resistivity model fitting. *Geotechnical and environmental geophysics* 1, 51–74.
- Lapenna, V., Lorenzo, P., Perrone, A., Piscitelli, S., Sdao, F., Rizzo, E., 2003. High-resolution geoelectrical tomographies in the study of Giarossa landslide (southern Italy). *Bull. Eng. Geol. Environ.* 62, 259–268. <https://doi.org/10.1007/s10064-002-0184-z>.
- Larson, H.J., 1975. *Statistics: An Introduction*. Wiley, New York, pp. 15.
- Lebourg, T., Binet, S., Tric, E., Jomard, H., El Bedoui, S., 2005. Geophysical survey to estimate the 3D sliding surface and the 4D evolution of the water pressure on part of a deep seated landslide. *Terra Nova* 17, 399–406. <https://doi.org/10.1111/j.1365-3121.2005.00623.x>.
- Lehmann, P., Gambazzi, F., Suski, B., Baron, L., Askarinejad, A., Springman, S.M., Holliger, K., Or, D., 2013. Evolution of soil wetting patterns preceding a hydrologically induced landslide inferred from electrical resistivity survey and point measurements of volumetric water content and pore water pressure. *Water Resour. Res.* 49, 7992–8004. <https://doi.org/10.1002/2013WR014560>.
- Leroy, P., Revil, A., 2009. A mechanistic model for the spectral induced polarization of clay materials. *J. Geophys. Res. Solid Earth* 114. <https://doi.org/10.1029/2008JB006114>. B10202.
- Leroy, P., Revil, A., Kemna, A., Cosenza, P., Ghorbani, A., 2008. Complex conductivity of water-saturated packs of glass beads. *J. Colloid Interface Sci.* 321 (1), 103–117. <https://doi.org/10.1016/j.jcis.2007.12.031>.
- Lesmes, D.P., Morgan, F.D., 2001. Dielectric spectroscopy of sedimentary rocks. *J. Geophys. Res.* 106 (B7), 2156–2202. <https://doi.org/10.1029/2000JB900402>.
- Lysdahl, A., Pfaffhuber, A.A., Anschutz, H., Kásin, K., Bazin, S., 2017. Helicopter electromagnetic scanning as a first step in regional quick clay mapping. *landslides in sensitive clays*. *Adv. Nat. Technol. Hazards Res.* 46, 475–485. [https://doi.org/10.1007/978-3-319-56487-6\\_39](https://doi.org/10.1007/978-3-319-56487-6_39).
- Malet, J.-P., Laigle, D., Remaître, A., Maquaire, O., 2005. Triggering conditions and mobility of debris flows associated to complex earthflows. *Geomorphology* 66 (1–4), 215–235. <https://doi.org/10.1016/j.geomorph.2004.09.014>.
- Marescot, L., Monnet, R., Chapellier, D., 2008. Resistivity and induced polarization surveys for slope instability studies in the Swiss Alps. *Eng. Geol.* 98, 18–28. <https://doi.org/10.1016/j.enggeo.2008.01.010>.
- Mauritsch, H.J., Seiberl, W., Arndt, R., Römer, A., Schneiderbauer, K., Sendhofer, G.P., 2000. Geophysical investigations of large landslides in the Carnic Region of southern Austria. *Eng. Geol.* 56 (3–4), 373–388. [https://doi.org/10.1016/S0013-7952\(99\)00120-9](https://doi.org/10.1016/S0013-7952(99)00120-9).
- McNeill, J.D., 1980a. *Electrical Conductivity of Soil and Rocks*. Technical Note TN-5. In: Geonics Ltd. Mississauga, Canada.
- McNeill, J.D., 1980b. *Electromagnetic Terrain Conductivity Measurement at Low Induction Numbers*. Technical Note TN-6. In: Geonics Ltd. Mississauga, Canada.
- Merritt, A.J., Chambers, J.E., Murphy, W., Wilkinson, P.B., West, L.J., Gunn, D.A., Meldrum, P.I., Kirkham, M., Dixon, N., 2014. 3D ground model development for an active landslide in Lias mudrocks using geophysical, remote sensing and geotechnical methods. *Landslides* 11, 537–550. <https://doi.org/10.1007/s10346-013-0409-1>.
- Mester, A., van der Kruk, J., Zimmermann, E., Vereecken, H., 2011. Quantitative Two-Layer Conductivity Inversion of Multi-Configuration Electromagnetic Induction Measurements. *Vadose Zone J.* 10, 1319–1330. <https://doi.org/10.2136/vzj2011.0035>.
- Morelli, G., Labrecque, D., 1996. Robust Scheme for ERT Inverse Modeling, Symposium on the Application of Geophysics to Engineering and Environmental Problems. 1996. pp. 629–638. <https://doi.org/10.4133/1.2922327>.
- Nakazato, H., Konishi, N., 2005. Subsurface structure exploration of wide area landslide by Aerial electromagnetic exploration. *Landslides* 2, 165–169. <https://doi.org/10.1007/s10346-005-0056-2>.
- Nturlagiannis, D., Robinson, J., Soupios, P., Slater, L., 2016. Field-scale electrical geophysics over an olive oil mill waste deposition site: evaluating the information content of resistivity versus induced polarization (IP) images for delineating the spatial extent of organic contamination. *J. Appl. Geophys.* 135, 418–426. <https://doi.org/10.1016/j.jappgeo.2016.01.017>.
- Pelton, W., Ward, S., Hallof, P., Sill, W., Nelson, P., 1978. Mineral discrimination and removal of inductive coupling with multifrequency ip. *Geophysics* 43, 588–609. <https://doi.org/10.1190/1.1440839>.
- Perrone, A., Lapenna, V., Piscitelli, S., 2014. Electrical resistivity tomography technique for landslide investigation: a review. *Earth-Sci. Rev.* 135, 65–82. <https://doi.org/10.1016/j.earscirev.2014.04.002>.
- Petley, D.N., Mantovani, F., Bulmer, M.H., Zannoni, A., 2005. The use of surface monitoring data for the interpretation of landslide movement patterns. *Geomorphology* 66 (1–4), 133–147. <https://doi.org/10.1016/j.geomorph.2004.09.011>.
- Petschko, H., Brenning, a., Bell, R., Goetz, J., Glade, T., 2014. Assessing the quality of landslide susceptibility maps – case study lower Austria. *Nat. Hazards Earth Syst. Sci.* 14, 95–118. <https://doi.org/10.5194/nhess-14-95-2014>, 2014.
- Portniaguine, O., Zhadanov, M.S., 1999. Focusing geophysical inversion images. *Geophysics* 64 (3), 874–887. <https://doi.org/10.1190/1.1444596>.
- Revil, A., Glover, P.W.J., 1998. Nature of surface electrical conductivity in natural sands, sandstones, and clays. *Geophys. Res. Lett.* 25 (1), 691–694. <https://doi.org/10.1029/98GL00296>.
- Revil, A., Koch, K., Holliger, K., 2012. Is it the grain size or the characteristic pore size that controls the induced polarization relaxation time of clean sands and sandstones? *Water Resour. Res.* 76, A31–A36. <https://doi.org/10.1029/2011WR011561>.
- Robinson, D.A., Abdu, H., Lebron, I., Jones, S.B., 2012. Imaging of hill-slope soil moisture wetting patterns in a semi-arid oak savanna catchment using time-lapse electromagnetic induction. *J. Hydrol.* 416, 39–49. <https://doi.org/10.1016/j.jhydrol.2011.11.034>.
- Rogers, N.W., Selby, M.J., 1980. Mechanisms of shallow translational landsliding during summer rainstorms: North Island, New Zealand. *Geograf. Ann. Ser. A, Phys. Geograph* 62, 11–21. <https://doi.org/10.2307/520448>.
- Ruttner, A., Schnabel, W., 1988. *Geologische Karte der Republik Österreich 1:50.000 Blatt 71 Ybbsitz*. In: *Geologische Bundesanstalt*. Wien.
- Samyn, K., Travelletti, J., Bitri, A., Grandjean, G., Malet, J.P., 2012. Characterization of a landslide geometry using 3D seismic refraction traveltome tomography: the La Valette landslide case history. *J. Appl. Geophys.* 86, 120–132. <https://doi.org/10.1016/j.jappgeo.2012.07.014>.
- Sass, O., Bell, R., Glade, T., 2008. Comparison of GPR, 2D-resistivity and traditional techniques for the subsurface exploration of the Oschingen landslide, Swabian Alb (Germany). *Geomorphology* 93, 89–103. <https://doi.org/10.1016/j.geomorph.2006.12.019>.
- Sastry, R.G., Mondal, S.K., Pachauri, A.K., 2012. *Combined Gravity and Electrical Imaging in Landslide Investigations at Narayan Bagar, Garhwal, Himalaya, India*. In: *25th symposium on the application of geophysics to engineering & environmental problems*, (March).
- Schnabel, W., Krenmayr, H.-G., Mandl, G.W., Nowotny, A., Roetzel, R., Scharbert, S., 2002. *Geol. Karte Niederöster. 1:200 000*. Geologische Bundesanstalt, Wien.
- Shanahan, P.W., Binley, A., Whalley, W.R., Watts, C.W., 2015. The use of Electromagnetic Induction to Monitor changes in Soil Moisture Profiles beneath Different Wheat Genotypes. *Soil Sci. Soc. Am. J.* 79, 459–466. <https://doi.org/10.2136/sssaj2014.09.0360>.
- Sirles, P., Haramy, K., Andrew, R.D., Surdahl, R.W., 2012. Seismic and electrical 3D imaging to aid in landslide remediation design, East Fork Landslide, Wolf Creek Pass., Colorado. *Geotech. Pract. Publ.* 7, 76–89. <https://doi.org/10.1061/9780784412633.0005>.
- Sirles, P., Haramy, K., Andrew, R.D., Surdahl, R.W., 2013. *Seismic and Electrical 3D Imaging to Aid in Landslide Remediation Design, East Fork Landslide, Wolf Creek Pass, Colorado*. In: *GeoChallenges: rising to the geotechnical challenges of Colorado*, pp. 76–89.
- Slater, L., 2007. Near surface electrical characterization of hydraulic conductivity: from petrophysical properties to aquifer geometries – a review. *Surv. Geophys.* 28 (2–3), 169–197. <https://doi.org/10.1007/s10712-007-9022-y>.
- Slater, L., Lesmes, D.P., 2002. Electrical-hydraulic relationships observed for unconsolidated sediments. *Water Resour. Res.* 38 (1213). <https://doi.org/10.1029/2001WR001075>.
- Slater, L., Binley, A.M., Daily, W., Johnson, R., 2000. Cross-hole electrical imaging of a controlled saline tracer injection. *J. Appl. Geophys.* 44 (2–3), 85–102. [https://doi.org/10.1016/S0926-9851\(00\)00002-1](https://doi.org/10.1016/S0926-9851(00)00002-1).
- Slater, L., Nturlagiannis, D., Wishart, D., 2006. On the relationship between induced polarization and surface area in metal-sand and clay-sand mixtures. *Geophysics* 71 (2), A1–A5. <https://doi.org/10.1190/1.2187707>.
- Sturges, H.A., 1926. The choice of a class interval. *J. Am. Stat. Assoc.* 21 (153), 65.
- Taboga, A., 2011. *Development of Integrated High-Resolution Geophysical, Photogrammetric and GPS Surveying Applied to Landslides in the South Wales Coalfield*. Cardiff University, United Kingdom.
- Titov, K., Tarasov, A., Ilyin, Y., Seleznev, N., Boyd, A., 2010. Relationships between induced polarization relaxation time and hydraulic properties of sandstone. *Geophys. J. Int.* 180, 1095–1106. <https://doi.org/10.1111/j.1365-246X.2009.04465.x>.
- Wainwright, H.M., Flores Orozco, A., Bücker, M., Dafflon, B., Chen, J., Hubbard, S.S., Williams, K.H., 2016. Hierarchical Bayesian method for mapping biogeochemical hot spots using induced polarization imaging. *Water Resour. Res.* 52, 533–551. <https://doi.org/10.1002/2015WR017763>.
- Ward, S., Hohmann, G., 1988. *Electromagnetic theory for geophysical applications*. *Electromagn. Meth. Appl. Geophys.* 1 (3), 130–311.
- Ward, Stanley H., 1990. Resistivity and induced polarization methods. *Geotech. Environ. Geophys.* 147–190. <https://doi.org/10.1190/1.9781560802785.ch6>.
- Weber, L., 1997. *Flächendeckende Beschreibung der Geologie von Österreich 1:500 000 im Vektorformat*. Exzerpt (Basiskarte Geologie) aus der Metallogenetischen Karte von Österreich 1:500 000. Geologische Bundesanstalt, Wien, Österreich.
- Weigand, M., Flores Orozco, A., Kemna, A., 2017. Reconstruction quality of SIP parameters in multi-frequency complex resistivity imaging. *Near Surface Geophysics* 15

- (2), 187–199. <https://doi.org/10.3997/1873-0604.2016050>.
- Weller, A., Slater, L., Nordsiek, S., Ntarlagiannis, D., 2010. On the estimation of specific surface per unit pore volume from induced polarization: a robust empirical relation fits multiple data sets. *Geophysics* 75 (4), WA105–WA112. <https://doi.org/10.1190/1.3471577>.
- Weller, A., Slater, L., Binley, A., Nordsiek, S., Shujie, X., 2015. Permeability prediction based on induced polarization: Insights from measurements on sandstone and unconsolidated samples spanning a wide permeability range. *Geophysics* 80 (2), D161–D173. <https://doi.org/10.1190/geo2014-0368.1>.
- Wessely, G., Draxler, I., Gangl, G., Gottschling, P., Heinrich, M., Hofmann, T., Lenhardt, W., Matura, A., Pavuza, R., Peresson, H., Sauer, R., 2006. *Geologie der österreichischen Bundesländer - Niederösterreich*. Geologische Bundesanstalt, Wien, Österreich.
- Zimmermann, E., Kemna, A., Berwix, J., Glaas, W., Vereecken, H., 2008. EIT measurement system with high phase accuracy for the imaging of spectral induced polarization properties of soils and sediments. *Meas. Sci. Technol.* 19 (9).